Combustion Theory and Modelling
Vol. 14, No. 6, 2010, 793–825

A computational framework for predicting laminar reactive flows with soot formation

Marc R.J. Charest*, Clinton P.T. Groth and Ömer L. Gülder

University of Toronto Institute for Aerospace Studies, 4925 Dufferin Street, Toronto, Ontario, Canada M3H 5T6

(*Received 11 February 2010; final version received 16 July 2010*)

Numerical modeling is an attractive option for cost-effective development of new high-efficiency, soot-free combustion devices. However, the inherent complexities of hydrocarbon combustion require that combustion models rely heavily on engineering approximations to remain computationally tractable. More efficient numerical algorithms for reacting flows are needed so that more realistic physics models can be used to provide quantitative soot predictions. A new, highly-scalable combustion modeling tool has been developed specifically for use on large multiprocessor computer architectures. The tool is capable of capturing complex processes such as detailed chemistry, molecular transport, radiation, and soot formation/destruction in laminar diffusion flames. The proposed algorithm represents the current state of the art in combustion modeling, making use of a second-order accurate finite-volume scheme and a parallel adaptive mesh refinement (AMR) algorithm on body-fitted, multiblock meshes. Radiation is modeled using the discrete ordinates method (DOM) to solve the radiative transfer equation and the statistical narrow-band correlated-*k* (SNBCK) method to quantify gas band absorption. At present, a semi-empirical model is used to predict the nucleation, growth, and oxidation of soot particles. The framework is applied to two laminar coflow diffusion flames which were previously studied numerically and experimentally. Both a weakly-sooting methane–air flame and a heavily-sooting ethylene–air flame are considered for validation purposes. Numerical predictions for these flames are verified with published experimental results and the parallel performance of the algorithm analyzed. The effects of grid resolution and gas-phase reaction mechanism on the overall flame solutions were also assessed. Reasonable agreement with experimental measurements was obtained for both flames for predictions of flame height, temperature and soot volume fraction. Overall, the algorithm displayed excellent strong scaling performance by achieving a parallel efficiency of 70% on 384 processors. The proposed algorithm proved to be a robust, highly-scalable solution method for sooting laminar flames.

Keywords: numerical modeling; laminar diffusion flames; soot formation; adaptive mesh refinement; parallel computation

1. Introduction

The combustion of hydrocarbon fuels in practical combustion devices such as industrial furnaces, gas turbine combustors, and diesel engines typically generates soot, which adversely affects performance and is detrimental to human health. Numerical modeling is an attractive option for the development of new high-efficiency and soot-free burner designs since

*Corresponding author. Email: charest@utias.utoronto.ca

ISSN: 1364-7830 print / 1741-3559 online

DOI: 10.1080/1364783.2010.512960
http://www.informaworld.com

it helps minimize costly trial-and-error experimentation. However, mathematical models representing realistic combusting flows must rely heavily on engineering approximations to ensure that computations remain tractable. Hydrocarbon combustion is inherently complex and these approximate models are not accurate enough to capture the interactions between gas-phase chemistry, turbulence, radiation transport, soot formation/oxidation, and multi-phase transport. As such, efficient numerical algorithms for reacting flows are needed so that realistic physics models can be used to provide quantitative soot predictions. These algorithms should exploit state-of-the-art numerical methods such as adaptive mesh refinement (AMR), high-order discretization schemes, and implicit nonlinear relaxation/time-evolution schemes. They should also take advantage of today's trend towards large-scale parallel computing. In this study, a new highly-scalable finite-volume scheme for predicting laminar reactive flows with detailed chemistry, radiation, and soot formation/destruction is formulated and described.

A low-cost numerical framework for solving laminar reacting flows was developed by Ern *et al*. [1] and later applied to the study of soot formation [2]. This framework solves the vorticity–velocity formulation of the Navier–Stokes equations in the low-Mach-number limit on adaptively refined meshes. Velocity–vorticity formulations automatically satisfy the divergence-free condition and cope with the velocity–pressure coupling by eliminating the pressure gradient term from the momentum equations. They do not require staggered meshes, are easily applied to non-orthogonal curvilinear coordinates, and can be solved with standard techniques. However, one drawback of velocity–vorticity formulations is the difficulty in accurately treating boundary conditions as appropriate values for the vorticity are not always known at the boundary [3].

The framework developed by Ern *et al*. [1] used a damped Newton method [4], a Krylov-based linear matrix solver, and an implicit Euler time-marching scheme for startup. It was applied in parallel on multiple processors via domain decomposition to reduce the overall solution time. Moderate scaling was achieved with a parallel efficiency of 64% on 16 processors (relative to four). This performance is largely attributed to the lack of a global preconditioner. Additionally, the domain decomposition was only performed in one direction which strongly limits the degree of partitioning of the problem and is generally not applicable for more complex geometry.

Smooke *et al*. [2] later added detailed descriptions for soot formation and oxidation based on a sectional representation of the aerosol dynamics [5]. Radiative losses from CO, CO_2, H_2O and soot emission were accounted for with the optically thin approximation (OTA). When the authors compared numerical and experimental results for a methane–air coflow diffusion flame, they obtained good agreement for temperature and soot but only moderate agreement for CH_4 and C_2H_2. Problems were initially experienced predicting bulk flame properties and thus inlet temperatures were increased to improve the predictions. More complex calculations were performed by Smooke *et al*. [6] using the discrete transfer method (DTM) [7] and a narrow-band approximation for the absorption spectrum [8].

Dworkin *et al*. [9] proposed improvements to the velocity–vorticity formulation of Ern *et al*. [1] that reduced spurious mass losses/gains for flows with large vorticity gradients. Despite these improvements, the approach does not fully conserve mass and introduces additional numerical instabilities. The modified formulation was applied to the transient analysis of soot formation in laminar coflow diffusion flames using a sectional aerosol representation [10].

A numerical framework for studying hydrocarbon growth in laminar coflow diffusion flames was developed by D'Anna and coworkers [11]. Conservation equations are solved in two dimensions using a first-order finite-volume advective scheme [12] and radiation was modeled with the DTM [7]. Major simplifications include the use of

empirically-tuned gray absorption coefficients and approximate transport properties based on nitrogen. The solver employed an alternating-direction implicit (ADI) scheme and a tri-diagonal matrix algorithm (TDMA) to relax the linearized equations. A point-wise Newton–Raphson scheme has also been used [13]. Soot formation/oxidation was later included using a moment model [14] and a sectional model [15].

Liu *et al*. [16] and Guo *et al*. [17] have also developed a mathematical model for studying soot formation in laminar coflow diffusion flames. Their implementation solves the primitive form of the governing equations for mass, momentum, energy and species conservation in the low-Mach-number limit on structured meshes. Two additional equations were solved for the conservation of soot mass and number as per the monodisperse soot models proposed by Fairweather *et al*. [18] and Leung *et al*. [19]. Radiation was modeled with the discrete ordinates method (DOM) [20] and a wide-band model for the gas absorption properties [21]. As with previous investigators, the soot spectral absorption coefficient was determined from Rayleigh scattering theory. Solutions were obtained using the SIMPLE finite-volume scheme which decouples the mass and momentum equations to deal with pressure-velocity couplings [22]. Their overall algorithm solves the equations in a decoupled manner by first solving for mass, momentum and energy using a TDMA. The equations for the individual gas-phase species masses, soot mass, and soot number density are then solved with a multigrid method [23]. This method is not applicable for time accurate studies and the employed low-Mach-number assumption limits its applicable range of operating conditions. Recently, Zhang and coworkers [24] have extended the framework to utilize an advanced fixed-sectional aerosol model. The original solution algorithm was modified to deal with the stiff nature of the soot transport equations and parallel implementation was carried out via a simple domain decomposition in one coordinate direction. The predictions of the modified scheme agree well with experimental measurements and reasonable parallel performance was achieved. Although such a domain decomposition of the problem cannot be carried out to large numbers of processors, a parallel efficiency of 82% was achieved on 12 processors.

While not specifically designed for the study of soot formation, Day and Bell [25] developed a highly efficient parallel solution algorithm. They have studied both steady and time-dependant complex reacting flows by solving the low-Mach-number form of the compressible flow equations. Borrowing from Pember *et al*. [26], the scheme employs a fractional step method and AMR to solve the equations on a single grid. Excellent parallel performance up to 4096 processors was observed when the scheme was applied to turbulent flames [27]. A major drawback of this particular framework is the restriction to low-Mach-number flows as the equation of state is only satisfied to order Mach number squared.

In this research, a new framework for the study of soot formation in complex reacting laminar flows is presented. It solves the unmodified equations governing compressible flows which are applicable for all speeds with a Newton–Krylov-based implicit solver. Discretization is performed using a high-order upwind-reconstructed finite-volume scheme on multiblock, body-fitted meshes with AMR. Soot is modeled as monodisperse with a simple acetylene-based kinetic mechanism for nucleation, growth, coagulation, and oxidation. The effects of both gas and soot emission/absorption are included using the DOM coupled with a wide-band formulation for the gas absorption coefficients. This framework extends the previous work of Northrup and Groth [28, 29] and provides a robust, highly-scalable solution method for sooting laminar flames. Details of the proposed solution method are presented and verification is sought via comparisons to published experimental and numerical results for two laminar coflow diffusion flames. Following this, the performance of the new algorithm is assessed to demonstrate its general applicability and potential for performing large-scale, detailed combustion computations.

2. Governing equations

Gaseous combusting laminar flow is described herein mathematically using the conservation equations for continuous, multicomponent, compressible, thermally-perfect mixtures of gases [30]. The equations consist of the conservation of total mass, individual species mass, mixture momentum, and mixture energy. However, modeling soot formation and destruction in gaseous combustion requires tracking an additional solid phase and capturing the interactions that occur between phases. An approach similar those developed by Leung *et al*. [19] and Fairweather *et al*. [18] is used in this work. In this approach, the soot particle size distribution is approximated by an average size that varied via surface reactions and coagulation. The representation requires only two additional transport equations for soot mass and number.

Assuming Newtonian flow, the conservation of global mass, momentum, energy, individual species mass, soot mass, and particle number can be summarized as

$$\frac{\partial \rho}{\partial t} + \nabla \cdot (\rho \mathbf{v}) = 0 \tag{1}$$

$$\frac{\partial}{\partial t}(\rho \mathbf{v}) + \nabla \cdot (\rho \mathbf{v}\mathbf{v} + p\mathbf{I}) = \nabla \cdot \boldsymbol{\tau} + \rho \mathbf{g} \tag{2}$$

$$\frac{\partial}{\partial t}(\rho e) + \nabla \cdot \left[\rho \mathbf{v}\left(e + \frac{p}{\rho}\right)\right] = \nabla \cdot (\mathbf{v} \cdot \boldsymbol{\tau}) - \nabla \cdot \mathbf{q} + \rho \mathbf{g} \cdot \mathbf{v} \tag{3}$$

$$\frac{\partial}{\partial t}(\rho Y_k) + \nabla \cdot [\rho Y_k(\mathbf{v} + \mathbf{V}_k)] = \dot{\omega}_k, \quad k = 1, \ldots, N \tag{4}$$

$$\frac{\partial}{\partial t}(\rho Y_\mathrm{s}) + \nabla \cdot [\rho Y_\mathrm{s}(\mathbf{v} + \mathbf{V}_Y)] = S_Y \tag{5}$$

$$\frac{\partial}{\partial t}(\rho N_\mathrm{s}) + \nabla \cdot [\rho N_\mathrm{s}(\mathbf{v} + \mathbf{V}_N)] = S_N \tag{6}$$

where t is the time, ρ is the mixture density, p is the total mixture pressure, $\mathbf{v}$ is the mixture velocity vector, e is the total mixture energy, Y_k is the mass fraction of species k, Y_s is the mass fraction of soot, N_s is the soot number density (number of particles per unit mass of mixture), $\mathbf{V}_k$ is the diffusion velocity of gas species k, $\mathbf{V}_Y$ is the diffusion velocity related to soot mass, $\mathbf{V}_N$ is the diffusion velocity related to soot number, $\dot{\omega}_k$ is the time rate of change of the kth species mass, S_Y is the time rate of change of the soot mass, S_N is the time rate of change of the soot number, $\boldsymbol{\tau}$ is the fluid stress tensor, $\mathbf{g}$ is the acceleration vector due to gravity, N is the number of gaseous species in the mixture, and $\mathbf{q}$ is the heat flux vector. The time rate of change of gaseous species includes contributions from both gas-phase chemistry and soot surface reactions.

The density of the mixture was calculated using the following state equation

$$\rho = \frac{p}{R_\mathrm{u} T\left(\sum_{k=1}^{N} Y_k / M_k\right)} \tag{7}$$

where R_u is the universal gas constant, T is the temperature, and M_k is the species molar mass. The heat flux vector contains contributions from conduction, diffusion, and radiation.

It is given by

$$\mathbf{q} = -\kappa \nabla T + \rho \sum_{k=1}^{N+1} h_k Y_k \mathbf{V}_k + \mathbf{q}_{\text{rad}} \tag{8}$$

where κ is the mixture thermal conductivity, h_k is the individual species enthalpy, and $\mathbf{q}_{\text{rad}}$ is the radiative heat flux. In Equation (8), and throughout this work, the $(N + 1)$th species refers to soot. The enthalpy of soot was approximated using the properties of graphite.

Multispecies diffusion was modeled here using the first-order Hirschfelder–Curtiss approximation [31] while soot was assumed to diffuse primarily by thermophoresis using a model based on the limit of free-molecular flow [2]. The gas-phase diffusion velocity is given by

$$\mathbf{V}_k = -\frac{D_k}{Y_k} \nabla Y_k \tag{9}$$

where D_k is the individual species mixture averaged diffusion coefficient. In addition to contributions from thermophoresis, a small Fickian diffusive flux was included in the soot particle transport equations. This was required to enhance numerical stability even though the transport of soot via Brownian motion is generally negligible. A similar procedure was adopted by Kennedy *et al*. [32]. The resulting diffusion velocities for soot are

$$\mathbf{V}_Y = -\frac{D_{\text{s}}}{Y_{\text{s}}} \nabla Y_{\text{s}} + \mathbf{V}_{\text{T}} \tag{10}$$

$$\mathbf{V}_N = -\frac{D_{\text{s}}}{N_{\text{s}}} \nabla N_{\text{s}} + \mathbf{V}_{\text{T}} \tag{11}$$

where $D_{\text{s}} = 10^{-8}\,\text{m}\,\text{s}^{-2}$ is the soot diffusion coefficient. Similarly, Kennedy *et al*. [32] specified a diffusion coefficient for soot equal to 1% of the gas diffusivity. The thermophoretic velocity, $\mathbf{V}_{\text{T}}$, for the soot particles is [33]

$$\mathbf{V}_{\text{T}} = -0.55 \frac{\mu}{\rho T} \nabla T \tag{12}$$

where μ is the mixture dynamic viscosity.

2.1. *Soot chemistry model*

Soot formation and destruction was modeled using the simplified soot kinetics described by Liu *et al*. [16]. This model is based on the reduced soot mechanisms of Leung *et al*. [19] and Fairweather *et al*. [18] which describe the evolution of soot through basic steps for nucleation, surface growth, coagulation, and oxidation. Acetylene is assumed to be the

only precursor responsible for the presence of soot. The resulting mechanism is

$$\begin{aligned} C_2H_2 &\rightarrow 2C(s) + H_2 \\ C_2H_2 + n \cdot C(s) &\rightarrow (n+2) \cdot C(s) + H_2 \\ n \cdot C(s) &\rightarrow C_n(s) \\ C(s) + \frac{1}{2}O_2 &\rightarrow CO \\ C(s) + OH &\rightarrow CO + H \\ C(s) + O &\rightarrow CO \end{aligned}$$

It follows from the mechanism above that the source term in Equation (5) can be written as

$$S_Y = 2M_s(R_1 + R_2) - (2R_3 + R_4 + R_5)A_s \tag{13}$$

where M_s is the molar mass of soot (assumed equal to the molar mass of carbon, 12 kmol kg^{-1}) and A_s is the surface area of soot per unit volume of aerosol. The terms R_3, R_4, and R_5 are the soot oxidation rates for reactions involving O_2, OH, and O, respectively. The terms R_1 and R_2 are the soot nucleation and surface growth rates defined by

$$R_1 = k_1[C_2H_2] \tag{14}$$

$$R_2 = k_2 f(A_s)[C_2H_2] \tag{15}$$

The function $f(A_s)$ incorporates the dependence of soot surface growth on the soot surface area per unit volume, A_s. Proposed forms of $f(A_s)$ include: $f(A_s) = A_s^{0.5}$ [19] and $f(A_s) = A_s$ [18]. Here we have used the first relationship. The corresponding rate constants k_1 and k_2 are given by [16]

$$k_1 = 1000 \exp(-16\,103/T) \tag{16}$$

$$k_2 = 1750 \exp(-10\,064/T) \tag{17}$$

Surface area A_s is related to the soot mass and number density by

$$A_s = \pi \left(\frac{6}{\pi} \frac{1}{\rho_s} \frac{Y_s}{N_s} \right)^{2/3} (\rho N_s) \tag{18}$$

where ρ_s is the density of soot, taken to be 1900 kg m^{-3} [16]. The oxidation reaction rates per unit surface area are modeled by

$$R_3 = 120 \left\{ \frac{k_a X_{O_2} \chi}{1 + k_z X_{O_2}} + k_b X_{O_2} (1 - \chi) \right\}, \qquad \chi = \left\{ 1 + \frac{k_T}{k_b X_{O_2}} \right\}^{-1} \tag{19}$$

$$R_4 = \varphi_{OH} k_4 T^{-1/2} X_{OH} \tag{20}$$

$$R_5 = \varphi_O k_5 T^{-1/2} X_O \tag{21}$$

where X_{O_2}, X_{OH}, and X_O denote the mole fractions of O_2, OH and O. The collision efficiencies for OH, φ_{OH}, and O, φ_O, were both assumed equal to 0.2. The rate of soot oxidation by O_2 was based on the Nagle–Strickland–Constable model [34] with the rate constants k_a, k_b, k_z, k_T, and k_4 taken from Moss *et al*. [35]. The rate constant k_5 was equal to the value used by Bradley *et al*. [36].

The source term in Equation (6) represents the production and destruction of the soot particle number density with nucleation and agglomeration. It is modeled herein as follows:

$$S_N = \frac{2}{C_{\min}} N_a R_1 - 2C_a \left(\frac{6M_s}{\pi\rho_s}\right)^{1/6} \left(\frac{6k_B T}{\rho_s}\right) [C(s)]^{1/6} (\rho N_s)^{11/6} \tag{22}$$

where N_a is Avogadro's number (6.022×10^{26} kmol^{-1}), k_B is the Boltzmann constant (1.38×10^{-23} m^2 kg s^{-2} K^{-1}), $C_{\min} = 700$ is the number of carbon atoms in the incipient carbon particle, C_a is the agglomeration rate constant, and $[C(s)] = \rho Y_s / M_s$ is the molar concentration of soot. In this work, agglomeration was neglected ($C_a = 0$) based on recommendations made by Liu *et al*. [16] and Ezekoye and Zhang [37].

Several issues related to numerical stability and convergence were encountered using the previously described soot model. First, both S_Y and S_N are functions of Y_s and N_s raised to sub-unity powers. For example,

$$S_Y \propto Y_s^{1/3} N_s^{1/6} \quad \text{and} \quad S_N \propto Y_s^{1/6} \tag{23}$$

As a result, derivatives of S_Y and S_N with respect to Y_s or N_s become infinite as $Y_s \to 0$ and $N_s \to 0$. Additionally, oscillations in Y_s or N_s caused by round-off or numerical diffusion errors can produce large fluctuations in the source terms when Y_s and N_s are small. Both of these issues caused the proposed Newton–Krylov time-marching algorithm to stall. To overcome this stall, A_s was modified by applying a blending function to eliminate any on/off switching experienced by S_Y and smooth its derivative with respect to Y_s and N_s. The modified surface area is given by

$$A_s^* = \beta(Y_s)\beta(N_s)A_s \tag{24}$$

where the blending function, $\beta(x)$, is defined as

$$\beta(x) = 1.0 - \exp\left[-5\left(\frac{x}{10^{-6}}\right)^2\right] \tag{25}$$

The modification was applied by replacing A_s with A_s^* in Equations (13) and (15).

3. Radiation model

Detailed treatment of thermal radiation is necessary for accurate prediction of the flame structure, species concentrations, and formation of soot [38]. The discrete ordinates method (DOM) [20] was implemented to evaluate the radiation flux term in Equation (3). Spectral absorption coefficients for H_2O, CO_2, and CO were approximated using the wide-band model developed by Liu *et al*. [21] which is based on the statistical narrow-band correlated-*k* (SNBCK) method [39].

In the DOM, the directional dependence of the equation of transfer is discretized and integrals over the solid angle are approximated by numerical quadrature. The radiative

intensity field is represented by a set of M different directions in the polar and azimuthal coordinates. For a non-grey absorbing-emitting medium, the steady-state equation of transfer for a single wavelength and discrete direction of propagation is given by

$$\frac{\partial I_{\eta,m}}{\partial s} = \hat{\mathbf{s}}_m \cdot \nabla I_{\eta,m} = \kappa_\eta \left(I_{\mathrm{b}\eta} - I_{\eta,m} \right), \quad \text{for} \quad m = 1, \ldots, M \tag{26}$$

where η is the wavenumber, m is the direction index, $I_{\eta,m}$ is the spectral intensity in the direction of $\hat{\mathbf{s}}_m$, κ_η is the spectral absorption coefficient, and $I_{\mathrm{b}\eta}$ is the spectral blackbody intensity. Equation (26) is solved using the space-marching finite-volume approach of Carlson and Lathrop [20] with the T_3 angular quadrature scheme [40] and centered differences for the spatial derivatives. The simplified angular redistribution technique proposed by Jendoubi *et al*. [41] was adopted to evaluate the angular gradient which results from expanding the first term in Equation (26) for axisymmetric coordinate systems.

In the SNBCK method, the spectral domain is discretized into wavelength intervals of size $\Delta\eta$ within which $I_{\mathrm{b}\eta}$ can be assumed constant and the radiative transfer in each interval is computed. Radiative quantities are integrated over the narrow bands by introducing a cumulative distribution function for the absorption coefficient, $g(\kappa)$, that can be interpreted as a dimensionless wavenumber coordinate which varies monotonically from 0 to 1. The cumulative distribution function is derived by taking the inverse Laplace transformation of the statistical narrow-band transmissivity [39]. Integrating Equation (26) over each narrow band yields

$$\int_0^1 \frac{\partial I_{\Delta\eta,m}}{\partial s} \mathrm{d}g = \int_0^1 \kappa_{\Delta\eta}(g) \left(I_{\mathrm{b}\Delta\eta} - I_{\Delta\eta,m} \right) \mathrm{d}g \tag{27}$$

where the subscript, $\Delta\eta$, refers to the specific wavenumber interval. Using Gauss–Legendre quadrature, the DOM equation is solved for each quadrature point, g_i, and the spectrally integrated intensity for each band is computed from

$$\overline{I_{\Delta\eta,m}} = \sum_{i=1}^{N_\mathrm{g}} w_i I_{\Delta\eta,m}(g_i) \tag{28}$$

where N_g is the number of Gauss quadrature points and w_i are the weights. Four Gauss quadrature points were found to provide a reasonable balance between accuracy and computational expense.

After the DOM equation is solved for each direction m and quadrature point i in each band, the divergence of the radiative heat flux is then evaluated as

$$\nabla \cdot \mathbf{q}_\mathrm{rad} \approx \sum_{j=1}^{N_\mathrm{b}} \sum_{i=1}^{N_\mathrm{g}} w_i \kappa_{\Delta\eta_j}(g_i) \left(4\pi I_{\mathrm{b}\Delta\eta_j} - \sum_{m=1}^{M} \omega_m I_{\Delta\eta_j,m}(g_i) \right) \Delta\eta_j \tag{29a}$$

where N_b are the number of narrow bands, ω_m are the ordinate weights, and $\Delta\eta_j$ is the narrow band width for the jth spectral interval. The blackbody intensity within each range, $I_{\mathrm{b}\Delta\eta_j}$, is evaluated at the band center. In this study, the narrow-band data of Soufiani and Taine [42] for H_2O, CO_2, and CO was used to construct the cumulative distribution function. To reduce the number of unknowns required for non-gray radiation in mixtures, the three radiating gases are approximated by a single gas with effective narrow-band parameters based on the optically thin limit [43]. Additional computational savings are achieved by

combining bands to form several wide bands using the lumping procedure described by Liu *et al*. [21]. Based on the recommendations of Goutière *et al*. [44], a total of nine non-uniformly spaced wide bands are employed.

The soot spectral absorption coefficient is determined in the Rayleigh limit for small spherical particles and is given by [45]

$$\kappa_{\eta,\text{soot}} = C f_v \eta \tag{30}$$

where f_v is the soot volume fraction and C is an empirical constant. The constant C was taken to be 5.5, which is similar to the value used by Liu *et al*. [16].

4. Solution procedure

Numerical solutions of Equations (1)–(6) are obtained using the parallel, implicit, finite-volume scheme with block-based AMR previously developed by Groth and coworkers [46, 47]. The scheme solves conservation equations on body-fitted, multiblock, quadrilateral meshes. In this finite-volume approach, the physical domain is discretized into finite-sized computational cells and the integral forms of conservation laws are applied to each individual cell. For cell (i, j), as shown in Figure 1, the approach results in the following coupled system of nonlinear ordinary differential equations (ODEs) for cell-averaged solution quantities:

$$\frac{\mathrm{d}\mathbf{W}_{ij}}{\mathrm{d}t} = \left.\frac{\partial \mathbf{W}}{\partial \mathbf{U}}\right|_{ij} \cdot \left\{ -\frac{1}{A_{ij}} \sum_{\text{faces, } k} (\mathbf{F}_k \cdot \hat{\mathbf{n}}_k \Delta l_k)_{ij} + \mathbf{S}_{ij} \right\} \tag{31}$$

where

$$\mathbf{U}_{ij} = [\rho, \rho u, \rho v, \rho e, \rho Y_1, \ldots, \rho Y_N, \rho Y_\text{s}, \rho N_\text{s}]^\text{T}$$
$$\mathbf{W}_{ij} = [p, u, v, T, Y_1, \ldots, Y_N, Y_\text{s}, N_\text{s}]^\text{T}$$

are the cell-averaged conserved and primitive solution vectors, respectively, A_{ij} is the cell area, $\hat{\mathbf{n}}_k$ and Δl_k are the normal vector and edge length for the kth face, and $\mathbf{S}_{ij}$ is the source term which includes contributions from axisymmetric terms, gravitational forces, finite

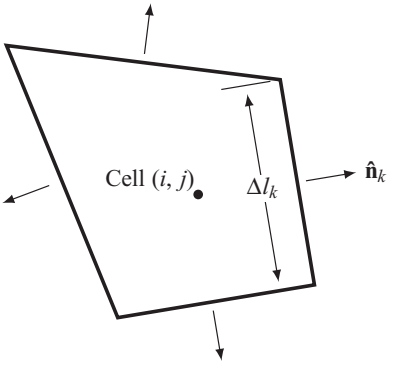

Figure 1. Two-dimensional quadrilateral computational cell.

rate-chemistry, and radiation. The numerical flux $\mathbf{F}_k = (\mathbf{F}, \mathbf{F}_\mathbf{v})$ comprises both inviscid, $\mathbf{F}$, and viscous, $\mathbf{F}_\mathbf{v}$, components which must be evaluated separately. The evaluation of these terms and the solution of Equation (31) are described in the following sections.

4.1. *Low-Mach-number preconditioning*

Solution of the nonlinear ODEs given by Equation (31) can be somewhat challenging as large differences between spatial and temporal scales can make the ODEs stiff. The stiffness of the ODEs is also significantly enhanced at very low flow speeds, which are of primary interest here, when the disparities between the convective and acoustic velocities become large [48]. Additionally, the nature of upwind discretizations for the inviscid fluxes can produce excessive dissipation at low speeds, corrupting overall solution accuracy.

Preconditioning replaces physical time derivatives with artificial ones in order to alter the speeds at which waves propagate. As per Weiss and Smith [49], application of the preconditioning to Equations (1)–(6) leads to the following system for axisymmetric coordinates:

$$\mathbf{\Gamma}\frac{\partial \mathbf{W}}{\partial t} + \frac{\partial}{\partial r}\mathbf{F} + \frac{\partial}{\partial z}\mathbf{G} = \frac{\partial}{\partial r}\mathbf{F}_\mathbf{v} + \frac{\partial}{\partial z}\mathbf{G}_\mathbf{v} + \mathbf{S} \tag{32}$$

where $\mathbf{\Gamma}$ is the preconditioning matrix for the primitive variables, $\mathbf{F}$ and $\mathbf{G}$ are the inviscid fluxes in the r- and z-directions, respectively, and $\mathbf{F}_\mathbf{v}$ and $\mathbf{G}_\mathbf{v}$ are the corresponding viscous fluxes. The preconditioning matrix, modified to include the equations for soot mass fraction and number density, is given by

$$\mathbf{\Gamma} = \begin{bmatrix}
\Theta & 0 & 0 & \rho_T & \rho_{Y_1} & \cdots & \rho_{Y_{N+1}} & 0 \\
u\Theta & \rho & 0 & u\rho_T & u\rho_{Y_1} & \cdots & u\rho_{Y_{N+1}} & 0 \\
v\Theta & 0 & \rho & v\rho_T & v\rho_{Y_1} & \cdots & v\rho_{Y_{N+1}} & 0 \\
H\Theta - (1-\rho h_p) & \rho u & \rho v & H\rho_T + \rho h_T & H\rho_{Y_1} + \rho h_{Y_1} & \cdots & H\rho_{Y_{N+1}} + \rho h_{Y_{N+1}} & 0 \\
Y_1\Theta & 0 & 0 & Y_1\rho_T & Y_1\rho_{Y_1} + \rho & \cdots & Y_1\rho_{Y_{N+1}} & 0 \\
\vdots & \vdots & \vdots & \vdots & \vdots & \ddots & \vdots & \vdots \\
Y_{N+1}\Theta & 0 & 0 & Y_{N+1}\rho_T & Y_{N+1}\rho_{Y_1} & \cdots & Y_{N+1}\rho_{Y_{N+1}} + \rho & 0 \\
N_\mathrm{s}\Theta & 0 & 0 & N_\mathrm{s}\rho_T & N_\mathrm{s}\rho_{Y_1} & \cdots & N_\mathrm{s}\rho_{Y_{N+1}} & \rho
\end{bmatrix} \tag{33}$$

where u and v are the r- and z-components of velocity, respectively, H is the total mixture enthalpy, and Θ is given by

$$\Theta = \frac{1}{V_\mathrm{p}^2} - \frac{\rho_T(1-h_p)}{\rho h_T} \tag{34}$$

The variables ρ_p, ρ_T, h_p, h_T, ρ_{Y_k}, and h_{Y_k} are thermodynamic quantities that describe the properties of the fluid. The subscripts denote partial derivatives. For a perfect gas, $\rho_p = 1/(RT), \rho_T = -\rho/T, h_T = c_p, h_p = 0, \rho_{Y_k} = -\rho M/M_k, h_{Y_k} = h_k$, R is the mixture ideal gas constant, M is mixture molar mass, and c_p is the mixture specific heat. The eigenvalues for the preconditioned Jacobian matrix in the r-direction, $\mathbf{\Gamma}^{-1}\partial\mathbf{F}/\partial\mathbf{W}$, become:

$$\lambda = \left[u' - a',\, u,\, u,\, u' + a',\, u,\, \ldots,\, u\right]^\mathrm{T} \tag{35}$$

where

$$u' = u\,(1-\alpha)$$
$$a' = \sqrt{\alpha^2 u^2 + V_{\mathrm{p}}^2}$$
$$\alpha = \frac{1}{2}\left(1-\beta V_{\mathrm{p}}^2\right)$$
$$\beta = \rho_p + \frac{\rho_T(1-h_p)}{\rho h_T}$$

The preconditioned velocity scale, V_{p}, is an artificial sound speed defined as

$$V_{\mathrm{p}} = \min[\,\max\left(V_{\mathrm{inv}},\ V_{\mathrm{pgr}},\ V_{\mathrm{vis}},\ M_{\mathrm{ref}}\cdot a\right),\ a\,] \tag{36}$$

where a is the speed of sound. The inviscid, pressure-gradient-induced, and viscous velocity scales, V_{inv}, V_{pgr}, and V_{vis}, respectively, are given by [49, 50]

$$V_{\mathrm{inv}} = \sqrt{u^2+v^2} \tag{37}$$

$$V_{\mathrm{pgr}} = \sqrt{\frac{|\Delta p|}{\rho}} \tag{38}$$

$$V_{\mathrm{vis}} = \frac{\mu/\rho}{\Delta x} \tag{39}$$

where Δp is the cell pressure gradient and Δx is the length of the computational cell. The term M_{ref} in Equation (36) is a reference Mach number included to prevent singularities at stagnation points. A value of 10^{-4} is used throughout this work.

4.2. *Round-off error control*

Another difficulty for flame computations with low flow velocities is the increasing significance of machine round-off errors that begin to denominate at Mach numbers below 10^{-3}. Following the procedure described by Choi and Merkle [51], a reference pressure, p_0, is introduced to minimize the influence of round-off errors at low Mach numbers. As a result, the pressure, p, is given by

$$p = p_0 + p' \tag{40}$$

where p_0 is a constant equal to the ambient pressure and p' represents the deviation of the local pressure from p_0. The reference pressure is subtracted from Equation (2) and p' replaces p in the definition of the solution vector, $\mathbf{W}$, when numerical solutions are sought.

4.3. *Inviscid flux evaluation*

To determine the numerical flux at the cell face, a high-order upwind Godunov scheme is used. Godunov's method [52] begins by assuming that the solution in each cell is piecewise-constant and that the intermediate solution state at the cell interface is approximated

by upwinding. It is this upwinding that ensures monotonicity of solutions and prevents unwanted oscillations. In two dimensions, given the left and right solution states, $\mathbf{W_L}$ and $\mathbf{W_R}$, the numerical flux the cell interface is defined as

$$\mathbf{F} \cdot \hat{\mathbf{n}} = \mathcal{F}(\mathbf{W_L}, \mathbf{W_R}, \hat{\mathbf{n}}) \tag{41}$$

where $\mathcal{F}$ is a flux function which solves a Riemann problem, $\mathcal{R}$, in a direction aligned along the face normal, $\hat{\mathbf{n}}$.

Roe's approximate Riemann solver was used throughout this work to evaluate the inviscid fluxes [53, 54]. Additionally, the correction proposed by Harten [55] was added to ensure that the entropy condition is never violated at the sonic point. The numerical flux in one direction is given by

$$\mathbf{F}(\mathcal{R}(\mathbf{W_L}, \mathbf{W_R})) = \frac{1}{2}(\mathbf{F_R} + \mathbf{F_L}) - \frac{1}{2}|\hat{\mathbf{A}}|\Delta\mathbf{W} \tag{42}$$

where $\mathbf{F_L}$ and $\mathbf{F_R}$ are the inviscid fluxes evaluated based on $\mathbf{W_L}$ and $\mathbf{W_R}$, $\Delta\mathbf{W} = \mathbf{W_R} - \mathbf{W_L}$, $|\hat{\mathbf{A}}| = \hat{\mathbf{R}}|\hat{\mathbf{\Lambda}}|\hat{\mathbf{R}}^{-1}$, $\hat{\mathbf{R}}$ is the matrix of primitive variable right eigenvectors and $\hat{\mathbf{\Lambda}}$ is the eigenvalue matrix. The matrix $\hat{\mathbf{A}}$ is the linearized flux Jacobian evaluated at a reference state, $\hat{\mathbf{W}}$. For simplicity, a reference state which relaxes Roe's conditions is used when dealing with multispecies, reacting flows [56, 57]. As such, the Roe-averaged flow variables, $\hat{f}$, are defined in terms of a mass weighting of the left and right flow variables, f_L and f_R, as given by

$$\hat{f} = \frac{\rho_R f_R + \rho_L f_L}{\rho_R + \rho_L} \tag{43}$$

where f_L and f_R can be any of the variables u, v, h, Y_k, Y_s, and N_s. The Roe-average density is given by $\hat{\rho} = \sqrt{\rho_R \rho_L}$.

The dissipation associated with the upwind discretization procedure can be controlled in the low-Mach-number limit by re-deriving Equation (42) based on the preconditioned wave speeds. Following the procedure outlined by Weiss and Smith [49], $|\hat{\mathbf{A}}|\Delta\mathbf{W}$ in Equation (42) is modified as follows:

$$|\hat{\mathbf{A}}|\Delta\mathbf{W} \simeq \hat{\mathbf{A}}\Delta\mathbf{W} = \mathbf{\Gamma}\left(\mathbf{\Gamma}^{-1}\frac{\partial\mathbf{F}}{\partial\mathbf{W}}\right)\Delta\mathbf{W} = \mathbf{\Gamma}|\mathbf{A_\Gamma}|\Delta\mathbf{W} \tag{44}$$

where $|\mathbf{A_\Gamma}| = \mathbf{R_\Gamma}|\Lambda_\mathbf{\Gamma}|\mathbf{R_\Gamma}^{-1}$. The subscript $\mathbf{\Gamma}$ denotes that the matrix of eigenvectors and eigenvalues were derived based on the preconditioned system. The resulting numerical flux function has the form

$$\mathbf{F}(\mathcal{R}(\mathbf{W_L}, \mathbf{W_R})) = \frac{1}{2}(\mathbf{F_R} + \mathbf{F_L}) - \frac{1}{2}\mathbf{\Gamma}|\mathbf{A_\Gamma}|\Delta\mathbf{W} \tag{45}$$

and ensures the correct scaling of the numerical dissipation in the low-Mach-number limit.

4.4. *High-order spatial accuracy*

The extension of Godunov's scheme to second-order can prove challenging as second-order schemes with constant coefficients can generate unwanted non-physical oscillations near solution discontinuities or locations where the solution is under-resolved [58]. Godunov's

scheme is first-order because the projection of the cell-averaged solution in each cell occurs on piecewise-constant states. This projection is completely decoupled from the upwinding process and thus one can easily modify the spatial approximation to increase solution accuracy. For this work, second-order spatial accuracy is achieved by interpolating the solution state at the cell interface between two adjacent cells. Monotonicity is ensured by using slope limiters to control gradients and locally reduce the scheme to first-order as necessary, thereby damping out any over- and under-shoots in the reconstructed solution [59]. In two dimensions, the reconstructed left and right states for interface $(i + \frac{1}{2}, j)$ are

$$\mathbf{W_L} = \mathbf{W}_{ij} + \phi_{ij} \left[\left. \frac{\partial \mathbf{W}}{\partial r} \right|_{ij} (r_{i+\frac{1}{2},j} - r_{ij}) + \left. \frac{\partial \mathbf{W}}{\partial z} \right|_{ij} (z_{i+\frac{1}{2},j} - z_{ij}) \right] \tag{46}$$

$$\mathbf{W_R} = \mathbf{W}_{i+1,j} + \phi_{i+1,j} \left[\left. \frac{\partial \mathbf{W}}{\partial r} \right|_{i+1,j} (r_{i+\frac{1}{2},j} - r_{i+1,j}) + \left. \frac{\partial \mathbf{W}}{\partial z} \right|_{i+1,j} (z_{i+\frac{1}{2},j} - z_{i+1,j}) \right] \tag{47}$$

where ϕ is a slope limiter. Slope limiting is performed with a limiter specifically designed for use in multiple dimensions [60]. The cell gradients are computed using linear reconstruction from Green–Gauss theory [61].

4.5. *Viscous flux evaluation*

The centrally-weighted diamond-path method described by Coirier and Powell [62, 63] was employed to evaluate the viscous component of the numerical flux at the cell faces. The viscous component is given by

$$\mathbf{F_v} \cdot \mathbf{n} = \mathcal{G}(\mathbf{W}, \nabla \mathbf{W}, \mathbf{n}) \tag{48}$$

where $\mathcal{G}$ is the viscous flux function.

In the diamond-path method, the gradients at each face are found by applying the divergence theorem to a four-sided polygon, or diamond path, whose vertices are defined as shown in Figure 2. The four vertices correspond to the two neighboring cell centers and the nodes of the interface separating the two cells. While the solution data at the cell centers is easily interpreted from the cell averages, the solution state at the vertices

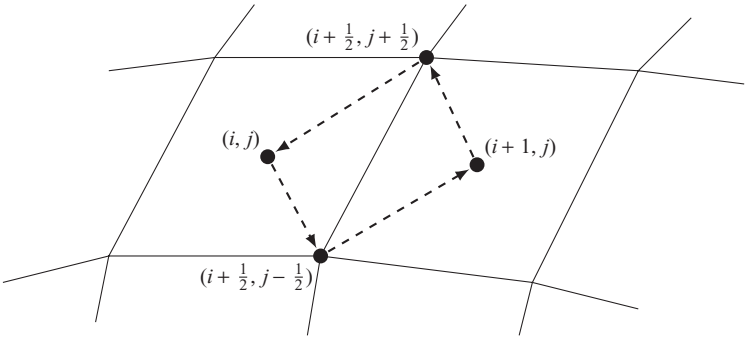

Figure 2. Diamond path viscous flux reconstruction for a quadrilateral cell.

must be interpolated. A linearity-preserving weighting scheme that linearly constructs the nodal data from the cell-centered solution states of the neighboring cells was used [64]. This diamond path technique avoids instabilities due to even/odd decoupling that occur in standard cell-centered formulations [62] and reduces to standard centered differences on Cartesian grids with uniform mesh spacing.

4.6. *Steady-state relaxation method*

Newton's method is applied to obtain steady-state solutions for the coupled set of nonlinear ODEs, given by Equations (1)–(6). It is used to relax the semi-discrete form of the governing equations to a steady-state solution such that

$$\mathbf{R}(\mathbf{W}) = \frac{\mathrm{d}\mathbf{W}}{\mathrm{d}t} = \mathbf{0} \tag{49}$$

The Newton algorithm developed by Groth and Northrup [65] specifically for use on large multiprocessor computer architectures is used here. The implementation makes use of a Jacobian-free inexact Newton method coupled with an iterative Krylov subspace linear solver. In Newton's method, a solution to Equation (49) is sought by iteratively solving a sequence of linear systems given an initial estimate, $\mathbf{W}^0$. Successively improved estimates are obtained by solving the linear system

$$\left(\frac{\partial \mathbf{R}}{\partial \mathbf{W}}\right)^n \Delta\mathbf{W}^n = \mathbf{J}(\mathbf{W}^n)\Delta\mathbf{W}^n = -\mathbf{R}(\mathbf{W}^n) \tag{50}$$

where $\mathbf{J} = \partial\mathbf{R}/\partial\mathbf{W}$ is the residual Jacobian. The improved solution at step n is then determined from

$$\mathbf{W}^{n+1} = \mathbf{W}^n + \Delta\mathbf{W}^n \tag{51}$$

The Newton iteration proceeds until some desired reduction in the norm of the residual is achieved and the condition $\|\mathbf{R}(\mathbf{W}^n)\| < \epsilon\|\mathbf{R}(\mathbf{W}^0)\|$ is met. The tolerance, ϵ, used in this work was 10^{-7}.

As mentioned, each step of Newton's method requires the solution of the linear problem

$$\mathbf{J}\mathbf{x} = \mathbf{b} \tag{52}$$

where $\mathbf{x} = \Delta\mathbf{W}$ and $\mathbf{b} = -\mathbf{R}(\mathbf{W})$. This system is relatively large, sparse, and non-symmetric. It is solved using the generalized minimal residual (GMRES) technique developed by Saad and coworkers [66–69], which is widely used for solving systems of this type. GMRES is an Arnoldi-based solution technique which generates orthogonal bases of the Krylov subspace to construct the solution. The technique is particularly attractive because the matrix **J** is not explicitly formed and instead only matrix-vector products are required at each iteration to create new trial vectors. This greatly reduces the required storage associated with forming **J** [70]. Termination also generally only requires solving the linear system to some specified tolerance, $\|\mathbf{R}^n + \mathbf{J}^n\Delta\mathbf{W}^n\| < \zeta\|\mathbf{R}(\mathbf{W}^n)\|$, where ζ is typically in the range 0.1–0.5 [71]. Lastly, a restarted version of the GMRES algorithm, GMRES(m), was used that minimizes storage by restarting every m iterations.

GMRES requires preconditioning to be effective. Right preconditioning the matrix **J** is performed to help facilitate the solution of Equation (52) without affecting the solution residual vector, **b**. The preconditioning takes the form

$$\left(\mathbf{J}\mathbf{M}^{-1}\right)(\mathbf{M}\mathbf{x}) = \mathbf{b} \tag{53}$$

where **M** is the preconditioning matrix. A combination of an additive Schwarz global preconditioner and a block incomplete lower-upper (BILU) local preconditioner is used which is easily implemented in the block-based AMR scheme. In additive Schwarz preconditioning, the solution in each block is updated simultaneously and shared boundary data is not updated until a full cycle of updates has been performed on all domains. The preconditioner is defined as follows

$$\mathbf{M}^{-1} = \sum_{k=1}^{N_\mathrm{B}} \mathbf{B}_k^T \mathbf{M}_k^{-1} \mathbf{B}_k \tag{54}$$

where N_B is the number of blocks and $\mathbf{B}_k$ is the gather matrix for the kth domain. The local preconditioner, $\mathbf{M}_k^{-1}$, in Equation (54) is based on block ILU(p) factorization [69] of the Jacobian for the first-order approximation of each domain. In this study, the level of fill, p, was maintained at four in order to minimize storage requirements.

Newton's method can fail when initial solution estimates fall outside the radius of convergence. To ensure global convergence of the algorithm, the implicit Euler startup procedure with switched evolution/relaxation (SER) that was proposed by Mulder and van Leer [72] was used. Application of this startup procedure to the semi-discrete form of the governing equations gives

$$\left[-\frac{\mathbf{\Gamma}}{\Delta t^n} + \left(\frac{\partial \mathbf{R}}{\partial \mathbf{W}}\right)^n\right] \Delta \mathbf{W}^n = -\mathbf{R}^n \tag{55}$$

where Δt^n is the time step. In the SER approach, the time step is varied from some small finite value and gradually increased as the steady state solution is approached. As $\Delta t^n \to \infty$, Newton's method is recovered.

In the quasi-Newton and SER methods, the time step size was determined by considering the inviscid Courant–Friedrichs–Lewy (CFL) and viscous Von Neumann stability criteria only. Time scales associated with gas-phase and soot chemistry were not incorporated into the time step size estimates. The time step size is determined by

$$\Delta t^n = \mathrm{CFL} \cdot \min\left[\frac{\Delta x}{u+a},\ \frac{\rho \Delta x^2}{\mu}\right] \tag{56}$$

where CFL is a constant greater than zero which determines the time step size. During the startup phase of the Newton calculation, a value for CFL between 10 and 100 is typically used.

4.7. *Parallel adaptive mesh refinement scheme*

Modeling practical combustion devices with complex chemistry, turbulence and radiation transport can quickly tax computational resources even on relatively coarse meshes. Unfortunately, high mesh densities are required in areas with steep gradients and small length

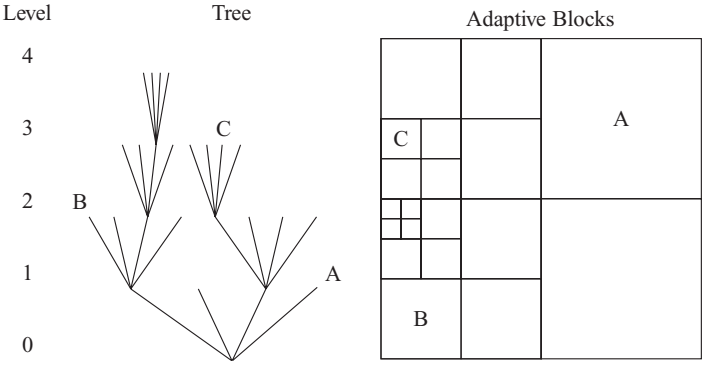

Figure 3. Adaptive mesh refinement quad-tree data structure and associated solution blocks for a quadrilateral mesh.

scales to accurately capture these processes. These locations can change over time and would normally require the use of large, fine uniform meshes. A flexible block-based AMR scheme is adopted here to limit the number of necessary computational cells by dynamically adapting the mesh to meet solution requirements. Details of the scheme and its implementation in parallel are described by Sachdev *et al*. [73, 74]. The extension of the scheme to three dimensions is described by Gao and Groth [75]. In this approach, block-based domain decomposition is applied to a body-fitted quadrilateral mesh. The grid blocks are organized in a hierarchical quad-tree data structure to facilitate automatic solution-directed mesh adaptation with physics-based criteria. The scheme borrows aspects from previous work by Berger and coworkers [76–79], Quirk [80], and De Zeeuw and Powell [81] for Cartesian grids, and has similarities with the block-based approaches described by Quirk and Hanebutte [82] and Berger and Saltzman [78].

Relaxation of Equation (31) with AMR proceeds as follows. The equations are first integrated forward in time on an initial structured, multiblock mesh to obtain updated volume-averaged solution quantities. The mesh is then adapted by coarsening or refining the blocks designated by the refinement criteria. A hierarchical tree-like data structure, shown in Figure 3, is used to retain connectivity between solution blocks and track their refinement history. The blocks requiring refinement are termed ‘parents’ and are divided into four new blocks called ‘children’. Each child is a new block with the same number of cells as its parent, doubling the mesh resolution in the region. Coarsening flagged blocks is carried out by reversing this process and combining four children into one single parent.

For reacting flows, refinement is based on the gradients of both species mass fractions and temperature. The refinement criteria employed here are defined by

$$\epsilon_1 \propto \frac{|\nabla T|}{T} \tag{57}$$

$$\epsilon_2 \propto |\nabla Y_k| \tag{58}$$

Based on either of these criteria, the mesh is refined and blocks are added wherever ϵ_1 or ϵ_2 are large. In the present work, grids were refined based on temperature in addition to fuel, acetylene, and soot mass fractions.

To further decrease the overall computational time, integration of the governing equations is performed in parallel. This is carried out by distributing the computational blocks

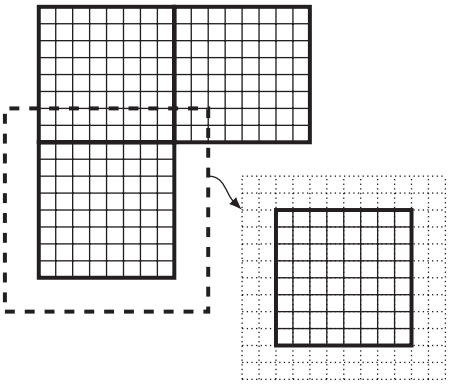

Figure 4. Sample multiblock grid and solution blocks depicting ghost cells.

among the available processors and simultaneously computing the solutions for each block on each processor. An even distribution of solution blocks is generally sought on homogeneous architectures while a weighted distribution is permissible for computations performed on heterogeneous systems such as networked workstations or computational grids. To ensure efficient load balancing, blocks are organized using a Morton ordering space filling curve which collocates nearest neighbors on the same processor [79]. This minimizes the amount of necessary communication and improves the overall parallel efficiency of the implementation. The proposed AMR scheme was implemented using the message passing interface (MPI) library and the C++ programming language [83].

As shown by Figure 4, ghost cells which surround the solution block and overlap cells on neighboring blocks are used to share solution content through inter-block communication. The conservation properties of the finite-volume discretization are retained across blocks with resolution changes by using the fine-grid interface flux to correct the flux computed on neighboring coarse blocks [76, 77]. Passing these flux corrections and the overlapping cell solution content between processors at each stage of the integration scheme accounts for the main source of inter-processor communication.

The serial nature of the space-marching technique employed in the DOM is problematic for large-scale parallel CFD solution algorithms. Several authors developed optimized sweeping procedures that simultaneously solve the DOM equations in different directions [84, 85]. However, they do not scale well to a large number of processors. A new highly-scalable time-marching algorithm for solving the DOM discretization of the radiative transfer equation was recently developed by Charest *et al*. [86]. However, this approach is not considered here. As such, no special treatment was implemented for solving the DOM equations. The DOM is solved in a parallel fashion at each time-step on the multiblock mesh along with Equations (1)–(6) by simultaneously sweeping all directions on the domain local to each processor. Solution content was shared among the processors by exchanging the state at the face-center of cells aligned with the block boundaries. Changes in mesh resolution were handled by linearly interpolating the coarse-mesh solution onto the fine-mesh and averaging the fine-mesh solution onto the coarse-mesh. Since the radiation solver employs a point-implicit space-marching technique, iteration is required to propagate information from upstream boundaries to downstream blocks. As a result, a penalty in terms of parallel efficiency was incurred because the number of iterations required to solve the radiation field increased with the number of blocks.

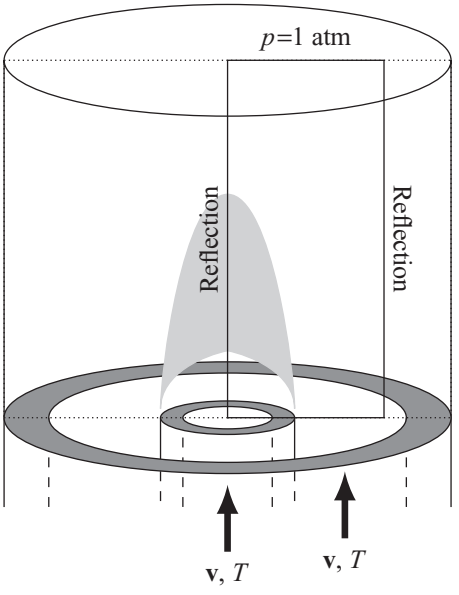

Figure 5. Schematic of laminar coflow diffusion flame.

5. Framework validation for laminar diffusion flames

In an effort to validate the proposed computational framework, two different laminar coflow diffusion flames were modeled under atmospheric conditions: the weakly-sooting methane–air flame studied extensively by Smooke *et al*. [2] and the heavily-sooting ethylene–air flame examined numerically by Liu *et al*. [16]. A schematic illustrating the computational domain and applied boundary conditions for both flames is provided in Figure 5. Reflection boundary conditions are applied along the centerline and in the far-field. At the outlet, temperature, velocity, species mass fractions, and soot number density are extrapolated while pressure is held fixed. The gas/soot mixture is specified at the inlet along with velocity and temperature while pressure is extrapolated. These boundary conditions where found to closely mimic boundary schemes based on a characteristic analysis [87].

The thermodynamic and transport properties were evaluated using CANTERA [88], an open-source software package for chemically-reacting flows. CANTERA was also used to compute the gas-phase kinetic rates.

5.1. *Methane–air flame*

For the methane–air flame, the burner configuration consisted of a central fuel tube with a 5.556 mm inner radius and a 0.794 mm wall thickness. Coflow air was supplied by a concentric tube of inner radius 47.625 mm. Both fuel and air were assumed to have uniform inlet velocity and temperature profiles with a fuel velocity of 5.5 cm s^{-1}, an air velocity of 12.54 cm s^{-1}, and an inlet temperature of 298 K. The original investigators [2] found that an inlet temperature of 420 K was required to obtain better agreement with the predicted flame height and local temperatures. This was later verified by Liu *et al*. [89] who also investigated this particular flame configuration numerically. The axisymmetric computational domain was rectangular with $0 \leq r \leq 47.625$ mm and $0 \leq z \leq 85$ mm and the initial mesh consisted of 72 cells in the r- and 112 in the z-direction for a total of

8064 cells. The initial mesh was divided amongst 96 blocks of 14 by 6 cells. The cells were clustered towards the centerline in the radial direction and towards the burner exit plane in the axial direction. Finite-rate chemistry was modeled using a modified version of the GRI-Mech 3.0 mechanism for CH_4 combustion [90]. In this modified version, N_2 was assumed inert and all reactions and species related to NO_x formation were removed. The final reduced mechanism consisted of 36 species and 219 reactions.

5.2. *Ethylene–air flame*

The heavily-sooting ethylene–air flame studied experimentally by Snelling *et al*. [91] and numerically by Liu *et al*. [16] used a configuration similar to the one described in the previous section. The burner fuel tube inner radius, wall thickness, and coflow-air tube inner radius are 4.45, 0.95, and 50 mm, respectively. Fuel and air are delivered at room temperature (294 K) with specified volume flow rates of 194 ml min^{-1} and 284 l min^{-1}. Unlike the methane flame, a parabolic laminar pipe flow velocity profile was assumed for the fuel inlet while a uniform velocity profile with a boundary layer along the outer fuel tube wall was assumed for the coflow air inlet. For this flame, the rectangular computational domain was defined in the range $0 \leq r \leq 30$ mm and $0 \leq z \leq 97.3$ mm with a similar initial grid to that used for the methane–air flame: 72 by 112 non-uniformly spaced cells divided into 96 blocks of 14 by 6 cells. The simulations were performed using the skeletal mechanism of Law [92] for ethylene–air combustion which consisted of 33 species and 205 elementary reactions. This mechanism was derived from the detailed mechanism proposed by Qin *et al*. [93] using a skeletal reduction technique which eliminates unimportant species and reactions based on a sensitivity analysis.

6. Numerical results

All computations were performed on a high performance parallel cluster consisting of 104 IBM P6-575 nodes with 128 GB RAM per node and a high-speed interconnect. The nodes each have 32 IBM POWER6 cores (4.7GHz) and are connected to a non-blocking switch with four 4x-DDR InfiniBand links.

For both flames, a converged solution was obtained on the initial 96 block mesh, the mesh was adapted, and then a new solution was obtained. This procedure was repeated and the meshes were adapted several more times to yield a final computational grid roughly 8–12 times the original size. Solutions were terminated when the two-norms of the mass, momentum, and energy residuals were reduced by approximately seven orders of magnitude. In the sections to follow, the grid convergence is discussed, the numerical predictions are verified, and the performance of the proposed algorithm is assessed.

6.1. *Adaptive mesh refinement*

The mesh statistics for each flame and level of refinement are given in Table 1. The table also provides the maximum predicted values for temperature and soot volume fraction in each calculation. For both flames, the maximum values converge asymptotically towards a final value. The minimum grid spacing for the finest mesh in the r- and z-directions are 0.017 and 0.009 mm for the methane flame and 0.017 and 0.01 mm for the ethylene flame, respectively.

The mesh adaption process is illustrated in Figures 6(a) and 6(b) for the methane– and ethylene–air flames, respectively. These figures depict the mesh solution blocks at

Table 1. Mesh statistics for both flames.

	Methane–air				Ethylene–air			
Level	Blocks	Cells	$T_{\max}$ (K)	$f_{v,\max} \times 10^7$	Blocks	Cells	$T_{\max}$ (K)	$f_{v,\max} \times 10^6$
0	96	8064	2010.43	8.50	96	8064	2102.01	8.46
1	144	12096	2012.53	8.77	159	13356	2103.53	8.55
2	294	24696	2013.33	8.86	282	23688	2103.06	8.58
3	462	38808	2013.69	8.92	402	33768	2104.30	8.63
4	765	64260	2013.68	8.92	822	69048	2104.09	8.60
5					1167	98028	2104.07	8.61

each level of refinement superimposed upon contours of soot volume fraction. In both cases, the AMR algorithm correctly identified the locations with high gradients and locally refined the mesh in the corresponding areas. This resulted in substantial reductions in computational cost and storage since equivalent uniform meshes with the same resolution as the finest meshes would require approximately 535 500 and 515 937 cells for the methane and ethylene flames, respectively. This corresponds to a factor of 5 and 8 reduction in mesh size.

In both cases, refinement occurred primarily in regions with high soot mass fraction gradients. Additional blocks were identified for refinement in the ethylene–air case. These blocks were outside the high-soot region and near the outer radius of the flame where temperature gradients were steep. Temperature gradients in the ethylene–air flame were much larger compared to the methane–air flame due to increased radiative heat losses to the surroundings. This increased radiative heat loss in the ethylene–air flame was confirmed by comparing the predicted $\nabla \cdot \mathbf{q}_{\text{rad}}$ for the two flames. It was approximately four times larger in the ethylene flame as compared to the methane flame.

Further investigation revealed that the finest mesh used in the ethylene–air case was possibly over-refined in the high-temperature-gradient areas. Cells were added along the flame sheet (defined by the peak temperature) where temperature gradients are high. However, temperature varies almost linearly with radius on both sides of the peak, Figure 9(a). As such, fewer cells are required to resolve these gradients near the peak since the second-order scheme is capable of accurately resolving them with few cells. While the ϵ_1 refinement criteria (Equation 57) may be easily adjusted to reduce the amount of refinement with respect to temperature gradients, such an adjustment is case-specific and therefore not performed here. These results emphasize the importance of improved error-based mesh adaptation techniques that do not rely on gradient- or physics-based refinement criteria [94, 95]. This is especially relevant for reacting flows which have a large numbers of chemical species and where the most effective refinement criterion is not readily apparent.

To further investigate the effect of grid resolution, predicted radial profiles of soot volume fraction as a function of mesh refinement level were compared in Figure 7. For the methane–air flame, illustrated in Figure 7(a), the profile along $z = 27.5$ mm clearly converges asymptotically after three levels of refinement. It is also evident that the minimum mesh spacing of 0.2 mm in the radial direction used by Liu *et al*. [89] for the same flame is not sufficient to fully describe the soot volume fraction peaks. Grid convergence is not strictly obtained for the ethylene–air flame, illustrated in Figure 7(b), as slight changes in the profile along $z = 30$ mm are still observed after the final refinement operation. The differences in the grid convergence characteristics between the two sets of flame

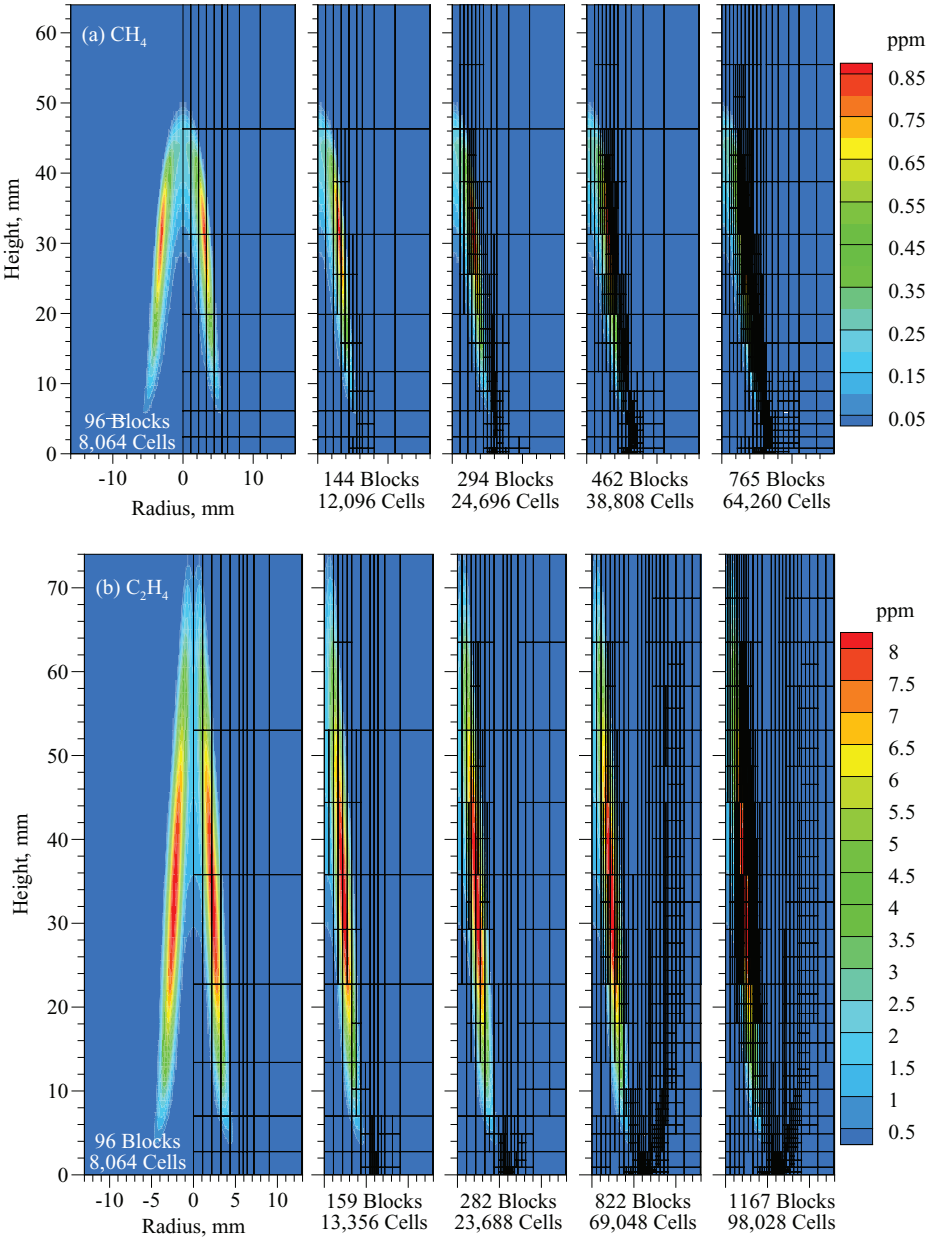

Figure 6. Refined multiblock computational mesh showing the solution blocks after each level of refinement superimposed on contours of soot volume fraction for (a) the CH_4 and (b) the C_2H_4 flame.

calculations are explained by comparing the contours for soot volume fraction depicted in Figures 6(a) and 6(b). The figures indicate that the number of mesh points in areas of high soot concentration is significantly lower in the ethylene flame and suggest that further refinement in these areas may be required.

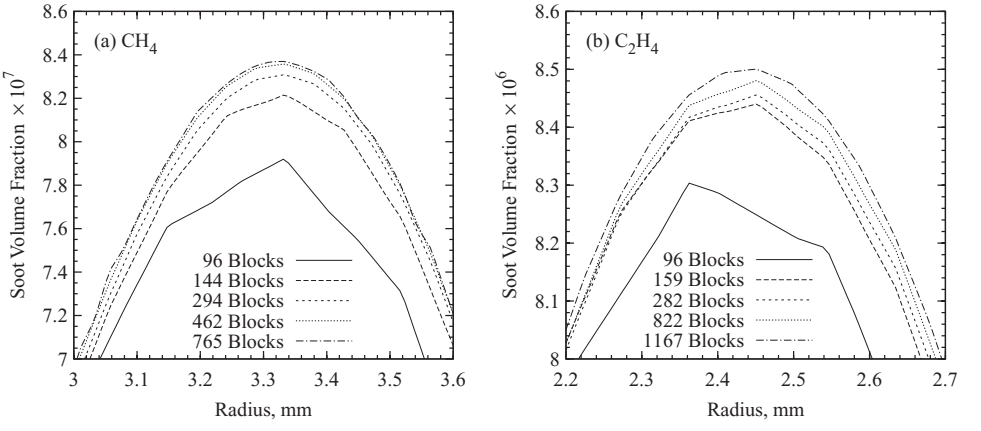

Figure 7. Effect of grid resolution on radial profiles of soot volume fraction for (a) the CH_4 flame at $z = 27.5$ mm and (b) the C_2H_4 flame at $z = 30$ mm.

6.2. *Comparison to experimental data*

6.2.1. *Methane flame*

The results for the methane flame were compared with the numerical and experimental results obtained by Smooke *et al*. [2] to verify and validate the models used. Overall, the flame structure is predicted reasonably well and the results are similar to those obtained by Smooke *et al*. [2]. Experimental measurements indicated that the flame height based on the location where the centerline temperature reached a maximum was 40 mm. The proposed framework slightly over-predicted the flame height based on temperature. A value of 55 mm is obtained here, which is similar to the predicted value of approximately 50 mm obtained by the previous investigators.

Predicted radial profiles for temperature, methane mole fraction, acetylene mole fraction, and soot volume fraction at various axial locations are compared with the previously published experimental measurements in Figure 8. The temperature profiles, Figure 8(a), are under-predicted by about 100–200 K along the centerline and over-predicted at the outer edges of the flame. Agreement between numerical and experimental results along the centerline is worse lower in the flame, at $z = 10$ mm, and improves with increasing axial distance from the burner exit plane. Similar agreement between numerical and experimental results are reported by Smooke *et al*. [2].

Comparisons between the predicted and measured radial profiles for methane and acetylene mole fraction are depicted in Figures 8(b) and 8(c), respectively. Although the general trends are captured, the quantitative agreement between experimental and numerical results is somewhat poor. Methane is over-predicted on average by a factor of 2 along the centerline and a factor of 4 at an axial height of 25 mm above the burner. Smooke *et al*. [2] obtained similar results and attributed this poor agreement to low computed flame temperatures, despite having increased inlet temperatures to improve predictions. As a result, methane is consumed at a slower rate and penetrates further downstream in the calculations. This poor agreement for the methane concentrations may also be a result of uncertainties at the fuel inlet boundary. Large gradients in methane concentration exist at the mouth of the burner which suggest that combustion may actually begin slightly upstream of the fuel tube exit plane. The predictions of acetylene concentration agree well with the measurements although the predicted profiles are narrower and the values along

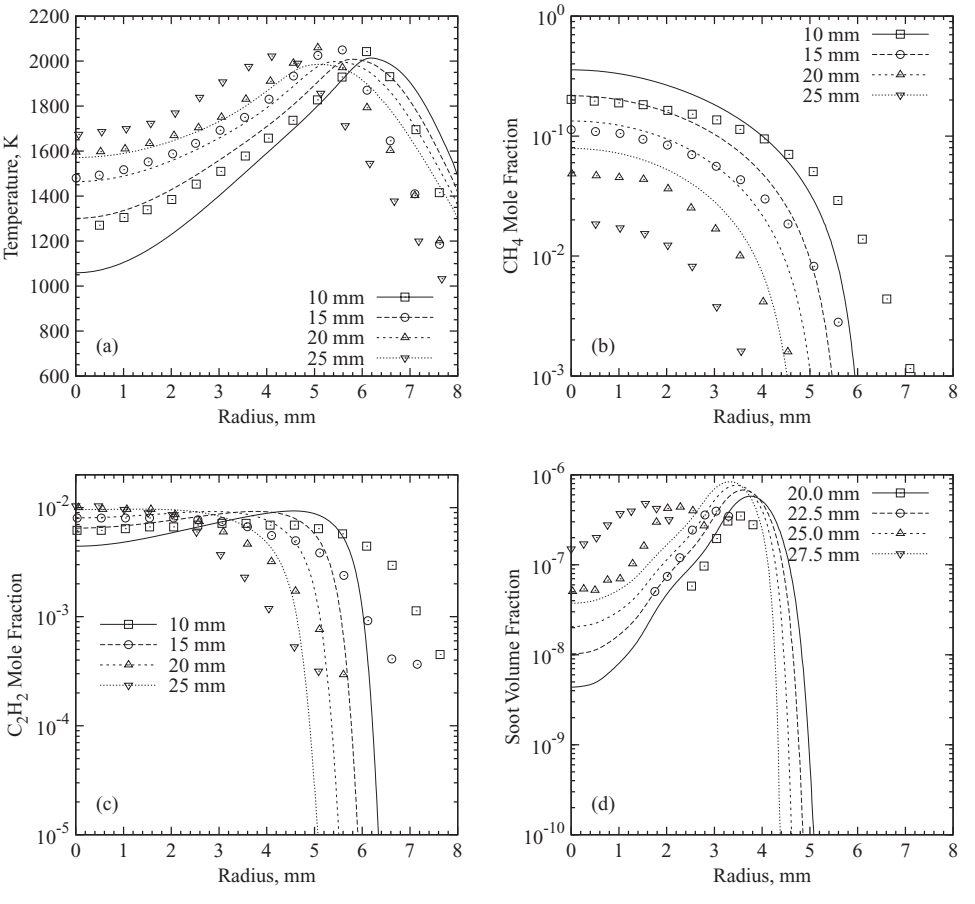

Figure 8. Comparison between the experimental measurements of Smooke *et al*. [2] (dots) and numerical predictions (lines) for (a) temperature, (b) CH_4 mole fraction, (c) C_2H_2 mole fraction, and (d) soot volume fraction for the methane–air laminar diffusion flame.

the centerline are slightly under-predicted. Acetylene concentrations rapidly vanish near the edges of the flame in the numerical results but measurements indicate that they slowly decrease. The under-prediction along the centerline may be a direct result of the delayed methane decomposition and under-predicted flame temperatures.

The predictions for soot volume fraction are compared with the measurements in Figure 8(d). A large improvement over the numerical results obtained by Smooke *et al*. [2] is observed which may be due to differences in the gas-phase and soot kinetics employed. The overall structure of soot is properly captured and the predicted values agree with experimental measurements. Smooke *et al*. [2] predicted a peak soot volume fraction three times larger than the measured value while the proposed framework only over-predicted by a factor of 1.7. These predicted peaks occurred in an annular region approximately 28 mm above the burner for Smooke *et al*. [2] and 33 mm here. Both numerical studies obtained values along the centerline that were a full order-of-magnitude lower than the experimentally measured values.

The predictions for the methane–air flame described in this section also agree with other numerical predictions obtained by Liu *et al*. [89] for the same flame. As with the original

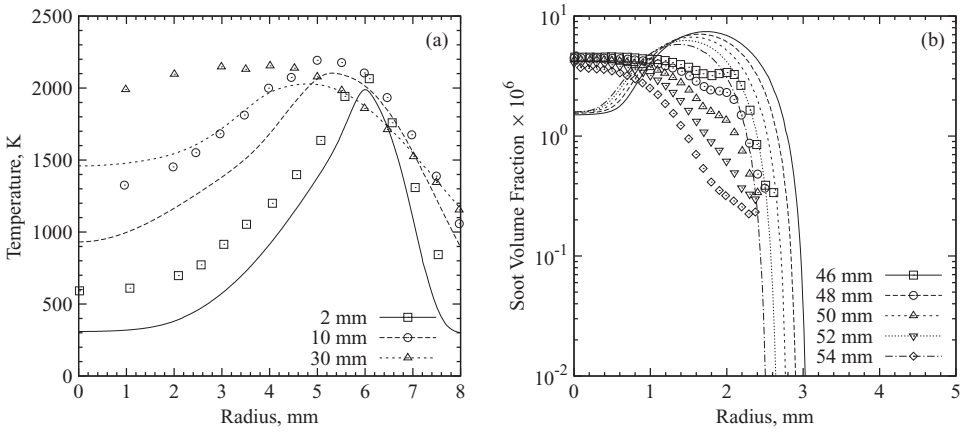

Figure 9. Comparison between the experimental measurements of Snelling *et al*. [91] (dots) and numerical predictions (lines) for (a) temperature, and (b) soot volume fraction for the ethylene–air laminar diffusion flame.

investigators, these authors used the artificially-increased fuel and air inlet temperatures to reduce the discrepancies between the predicted and measured peak flame temperatures.

6.2.2. *Ethylene flame*

The results obtained using the proposed algorithm are similar to those reported by Liu *et al*. [16]. Comparing the two sets of predictions, the computed temperature field in the present study is in slightly better quantitative agreement with the experimental measurements. The proposed framework calculated a peak temperature of 2104 K as compared to a measured peak of 2156 K and the prediction of 2010 K by Liu *et al*. [16]. The predicted radial profiles of temperature along selected axial heights are compared with the measurements in Figure 9(a). While the predicted temperature profiles agree well with the measurements near the peaks, the values near the centerline and outer portion of the flame are significantly under-predicted. These low predicted flame temperatures are attributed to the neglect of fuel preheating and other uncertainties in the inlet boundary conditions.

As shown in Figure 9(b), the predictions of soot volume fraction are also in reasonable quantitative agreement with the experimental measurements. A peak value of 8.6 ppm was predicted using the current implementation compared to the measured peak of 8.021 ppm. Liu *et al*. [16] obtained slightly better quantitative agreement, predicting a peak soot volume fraction of 8.0 ppm. The computed structure of the soot distributions differs significantly from the experimental results. This is observed in Figure 9(b), which compares the predicted soot volume fraction along various radial profiles with the previously published experimental measurements. The calculations predict a more annular structure with lower soot concentrations along the centerline than the measurements. Similar results were obtained by Liu *et al*. [16].

6.3. *Effect of gas phase mechanism*

Calculations of the ethylene–air flame with the initial coarse mesh were performed a second time using the modified form of GRI-Mech 3.0 to assess the sensitivity of soot formation to

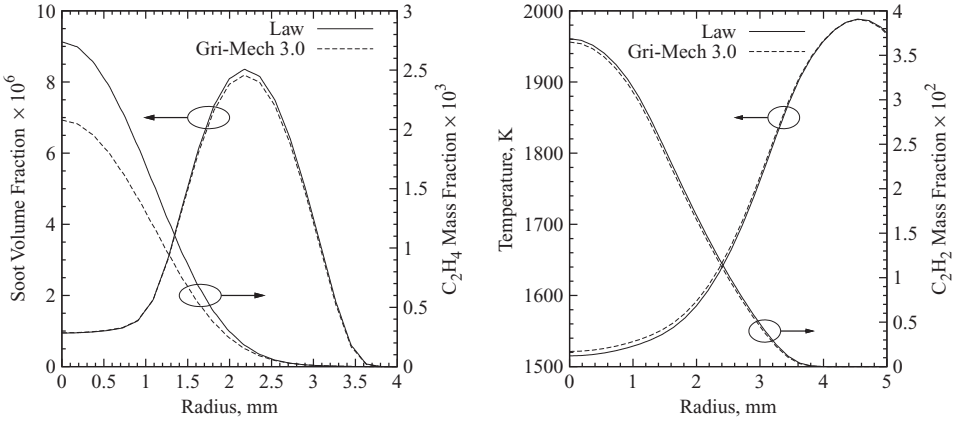

Figure 10. Predicted radial profiles of temperature, soot volume fraction, C_2H_2 and fuel mass fraction for the C_2H_4 flame at $z = 30$ mm obtained using different gas-phase mechanisms.

gas-phase kinetics. A comparison of the radial profiles along $z = 30$ mm for ethylene and acetylene mass fraction, temperature, and soot volume fraction which were obtained using both mechanisms is illustrated in Figure 10. Calculations using GRI-Mech 3.0 predicted a slightly lower peak soot volume fraction and a 25% lower centerline fuel mass fraction when compared to calculations using the skeletal mechanism of Law [92]. Negligible differences are observed between predictions for temperature and acetylene concentrations. The large differences in fuel mass fraction can be attributed to the higher laminar flame speeds predicted by GRI-Mech 3.0. Egolfopoulos and Dimotakis [96] found that this mechanism drastically over-predicted the laminar flame speeds in ethylene–air mixtures. In contrast, the skeletal mechanism of Law [92] was demonstrated to accurately reproduce laminar flame speeds under atmospheric conditions. Despite these large differences in the predicted ethylene concentrations, acetylene and soot concentrations are not affected by the change in mechanism.

6.4. *Parallel performance*

The parallel performance of the algorithm was assessed for both strong and weak scaling. These two properties are a measure of the ability to demonstrate a proportionate increase in parallel speedup with more processors. For the strong scaling test, the problem size is held fixed while the number of processors used to perform the computation is varied. Weak scaling is measured by holding the work load per processor fixed and varying the problem size with the number of processors. These two scaling properties are measured by the parallel speedup S_p and efficiency η_p which are defined as

$$S_p = \frac{t_1}{t_p} \tag{59}$$

$$\eta_p = \frac{S_p}{p} \tag{60}$$

where t_1 and t_p are the total wall times required to solve the problem with 1 and p processors, respectively.

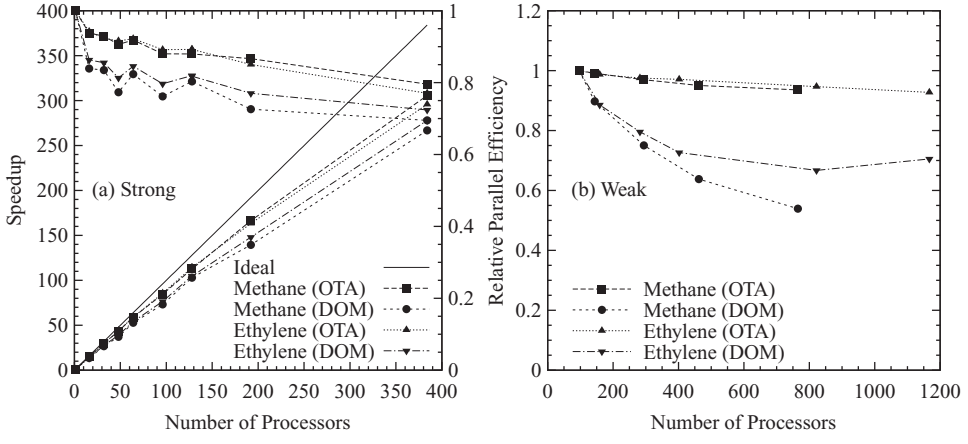

Figure 11. Parallel performance of the proposed solution algorithm showing the (a) strong and (b) weak scaling performance obtained for the methane- and ethylene–air laminar diffusion flame simulations.

In both the strong and weak scaling tests, solutions were also obtained using the OTA for radiative heat transfer [16]. The OTA assumes that radiation leaving a surface travels through the domain unattenuated. As a result, the radiative intensity field is known everywhere and $\nabla \cdot \mathbf{q}_{\text{rad}}$ can be evaluated directly without solving the radiative transfer equation. The parallel performance of the current DOM implementation is quantified by comparing the results using both the OTA and DOM.

6.4.1. *Strong scaling*

Strong scaling of the algorithm applied to both flames was measured using fixed-size meshes consisting of 384 equally-sized blocks of 14 by 6 cells (32 256 total cells). The work load per processor was varied without affecting the partitioning of the mesh by changing the number of blocks assigned to each processor. As a result, only the effect of inter-processor communication on parallel efficiency is taken into account. The negative effects of mesh partitioning on the effectiveness of Schwarz preconditioning and the parallel efficiency of the implemented DOM space-marching technique were neglected for this study.

The resulting relationship between parallel speedup, efficiency, and number of processors is shown in Figure 11(a) for the two flames. Excellent parallel performance is achieved with an efficiency greater than 70% up to 384 processors. Slight differences between the results for both flames exist which are caused by changes in governing equation stiffness with soot production and gas-phase kinetic mechanism. Comparing the results obtained using the two radiation models, the parallel performance of the overall algorithm improved when the OTA was used to evaluate $\nabla \cdot \mathbf{q}_{\text{rad}}$. Parallel efficiencies of 70 and 77% on 384 processors were obtained using the DOM and OTA, respectively. This improvement is attributed to the added communication required when solving the DOM equations. When using the DOM with the proposed algorithm, both the fluid solution for the surrounding ghost cells and the radiative intensities along the block boundaries are communicated. Only the fluid solution states are be passed when using the OTA.

Table 2. Wall-clock times for methane flame on 96-block mesh using 96 processors and various gas-phase reaction mechanisms.

Gas-phase mechanism	Gaseous species	Wall time (min)	Newton steps
Kazakov and Frenklach [97]	24	16.8	620
Gri-Mech 3.0	36	29.8	662
Appel *et al*. [98]	101	176.5	609

6.4.2. *Weak scaling*

The weak scaling performance of the proposed solution algorithm is observed in Figure 11(b) for the two different flames and radiation models. It was obtained by assigning each processor a single block and iterating for a fixed number of Newton steps. Due to the known performance degradation of the Newton–Krylov algorithm with number of solution blocks [65], true weak scaling should be measured by the time required to obtain a fully converged solution. However, weak scaling with full convergence was not carried out here. As a result, the procedure performed in this study only yields an approximate measure of weak scaling performance. The parallel inefficiencies of the DOM implementation are still accounted for since the DOM is fully converged at each Newton iteration.

When the OTA was used, excellent weak scaling performance is observed with a parallel efficiency of 92% achieved on 1167 processors. A significant reduction in parallel performance is observed when the DOM radiation model is used. Using the DOM, increasing the mesh size by a factor of 8 produced a two-fold decrease in parallel efficiency for the methane flame. This large decrease in parallel performance is due to the serial nature of the space-marching technique used to solve the DOM equations. The lowest parallel efficiencies achieved using the DOM were 54% for the methane–air flame on 765 processors and 67% for the ethylene–air flame on 822 processors.

6.4.3. *Computational cost for methane flame*

The computational cost as measured in terms of the wall-clock time for the methane flame calculations on the 96-block mesh (8064 cells) is provided in Table 2 for several different gas-phase mechanisms with varying levels of complexity. All computations use the DOM for radiation and solve the full set of governing equations (1)–(6). They were each started from the same initial guess. The results show that although wall time increases as more species are introduced to describe the gaseous phase, the number of Newton iterations remains virtually unaffected. This demonstrates the effectiveness of the Newton–Krylov approach advocated here. The calculation with 101 species is completed in less than three hours when 96 processors are used.

The performance of the proposed algorithm was also compared to similar numerical frameworks for studying soot that were discussed in Section 1. Zhang *et al*. [24] performed computations for the same methane flame that is studied here on a mesh with 16 512 cells using the modified version of GRI-Mech 3.0. They reported wall-clock times of 350 min to obtain converged flame solutions when soot was neglected using 12 processors with similar floating point performance as those used in the the present work. Assuming a 50% parallel efficiency on 96 processors (this a valid assumption since parallel performance decays exponentially as more processors are used [99]) and that computation time varies linearly with the number of cells, their solution algorithm is expected to take 35 min using 96 processors on a mesh with 8064 cells. The new algorithm proposed here required only

29.8 min to solve the full governing equations, which included soot. This would seem to provide a substantial reduction in the computational time required to perform detailed simulations of laminar flames since the estimated computation time for the solution method of Zhang *et al*. [24] does not include the additional cost of solving the equations governing soot. Additionally, the computational framework described herein provides a much more general approach for laminar flames by solving the unmodified, fully-compressible, gas-phase equations on complex domains using multiblock, body-fitted mesh. The proposed framework would also seem to offer similar performance improvements over the methodology proposed by Ern *et al*. [1]. Although, the comparison is made difficult by uncertainties in the relative computational performance of the computer processors used and because Earn *et al*. [1] only report wall-clock times for a portion of the overall solution.

7. Summary and future work

A new numerical framework for modeling laminar flames with detailed gas-phase chemistry, soot formation/oxidation, and radiative heat transfer has been developed. The framework uses a parallel implicit solver for fast, efficient solution and a block-based AMR scheme to capture small-scale processes on computationally tractable grids. Validation was performed by applying the framework to two different laminar coflow diffusion flames and evaluating the algorithm's predictive accuracy. Both a weakly-sooting methane–air and a heavily-sooting ethylene–air flame were studied. The effectiveness of the AMR procedure at providing grid-independent results in an efficient manner was shown. Although small changes in the radial soot volume fraction profile for the ethylene flame were still observed after the final level of refinement, grid-converged results were obtained for the most part for both the methane and ethylene flames. This was achieved with a substantial reduction in mesh size compared to meshes with uniform spacing. Good agreement with published experimental data for temperature and soot volume fraction was achieved in both cases. The algorithm demonstrated excellent strong scaling performance by achieving a parallel efficiency greater than 70% up to 384 processors. Outstanding weak scaling performance (92% parallel efficiency on 1167 processors) was observed when the OTA was used to model radiation. However, weak scaling performance degraded when the DOM was employed.

The algorithm proved to be a robust, accurate, and highly-scalable solution method for sooting laminar flames. It successfully tackled large problems using domain decomposition and effectively minimized the sizes of computational meshes using AMR. Future developments should focus on improving the scalability, refinement efficiency, and predictive accuracy of the algorithm. Since the main parallel inefficiencies were attributed to the space-marching DOM, advanced DOM solution techniques specifically designed for use on large, parallel architectures would significantly improve the proposed algorithm's scalability [86]. Refinement efficiency can be improved using more advanced a posteriori error estimates which do not rely solely on gradients of solution quantities [94, 95]. The currently employed gradient-based AMR criteria incorrectly flagged blocks for refinement in some cases where the solution was already adequately resolved. Lastly, the predictive accuracy of the proposed framework is improved by employing more realistic gas-phase chemistry and soot models. Detailed gas-phase kinetic mechanisms that describe the formation of large molecular weight soot precursors coupled with advanced descriptions for soot kinetics and aerosol dynamics were found to offer excellent quantitative predictions [15]. The enhanced computational efficiency offered by the proposed numerical scheme should allow tractable computations using these generally more advanced and complex chemical kinetic schemes and soot models.

Acknowledgements

We thank Dr. Fengshan Liu from the National Research Council (NRC) for his advice and discussions on this research. Operational funds for this work have been provided by the Natural Sciences and Engineering Research Council (NSERC) and the Canadian Space Agency (CSA). Computational resources for performing all of the calculations reported herein were provided by the SciNet High Performance Computing Consortium at the University of Toronto and Compute/Calcul Canada through funding from the Canada Foundation for Innovation (CFI) and the Province of Ontario, Canada.

References

[1] A. Ern, C.C. Douglas, and M.D. Smooke, *Detailed chemistry modeling of laminar diffusion flames on parallel computers*, Int. J. Supercomput. Ap. 9 (1995), pp. 167–186.

[2] M.D. Smooke, C.S. McEnally, L.D. Pfefferle, R.J. Hall, and M.B. Colket, *Computational and experimental study of soot formation in a coflow, laminar diffusion flame*, Combust. Flame 117 (1999), 117–139.

[3] C. Davies and P.W. Carpenter, *A novel velocity–vorticity formulation of the Navier–Stokes equations with applications to boundary layer disturbance evolution*, J. Comput. Phys. 172 (2001), pp. 119–165.

[4] P. Deuflhard, *A modified Newton method for the solution of ill-conditioned systems of nonlinear equations with application to multiple shooting*, Numer. Math. 22 (1974), pp. 289–315.

[5] R.J. Hall, M.D. Smooke, and M.B. Colket, *Prediction of soot dynamics in opposed jet diffusion flames*. In: F Dryer, R Sawyer (Eds.), Physical and Chemical Aspects of Combustion: A Tribute to Irvin Glassman. Amsterdam: Gordon & Breach, 1997, pp. 189–230.

[6] M.D. Smooke, M.B. Long, B.C. Connelly, M.B. Colket, and R.J. Hall, *Soot formation in laminar diffusion flames*, Combust. Flame 143 (2005), pp. 613–628.

[7] F.C. Lockwood and N.G. Shah, *A new radiation solution method for incorporation in general combustion prediction procedures*, Proc. Combust. Inst. 18(1) (1981), pp. 1405–1414.

[8] W.L. Grosshandler, *RADCAL: A narrow-band model for radiation calculations in a combustion environment*, NIST Technical Note 1402 (1993).

[9] S.B. Dworkin, B.A.V. Bennett, and M.D. Smooke, *A mass-conserving vorticity–velocity formulation with application to nonreacting and reacting flows*, J. Comput. Phys. 215 (2006), pp. 430–447.

[10] S.B. Dworkin, J.A. Cooke, B.A.V. Bennett, B.C. Connelly, M.B. Long, M.D. Smooke, R.J. Hall, and M.B. Colket, *Distributed-memory parallel computation of a forced, time-dependent, sooting, ethylene/air coflow diffusion flame*, Combust. Theor. Model. 13 (2009), pp. 795–822.

[11] A. D'Anna, A. D'Alessio, and J.H. Kent, *A computational study of hydrocarbon growth and the formation of aromatics in coflowing laminar diffusion flames*, Combust. Flame 125 (2001), pp. 1196–1206.

[12] W.J. Minkowycz, E.M. Sparrow, G.E. Schneider, and R.H. Pletcher, *Handbook of Numerical Heat Transfer*, John Wiley, New York, 1988.

[13] A. D'Anna and J.H. Kent, *Aromatic formation pathways in non-premixed methane flames*, Combust. Flame 132 (2003), pp. 715–722.

[14] A. D'Anna, G. Mazzotti, and J. Kent, *Modeling of particulate formation in a coflowing diffusion flame*, Combust. Sci. Tech. 176 (2004), pp. 753–767.

[15] A. D'Anna and J.H. Kent, *A model of particulate and species formation applied to laminar, nonpremixed flames for three aliphatic-hydrocarbon fuels*, Combust. Flame 152 (2008), pp. 573–587.

[16] F. Liu, H. Guo, G.J. Smallwood, and Ö.L. Gülder, *Effects of gas and soot radiation on soot formation in a coflow laminar ethylene diffusion flame*, J. Quant. Spectrosc. Radiat. Transfer 73 (2002), pp. 409–421.

[17] H. Guo, F. Liu, G.J. Smallwood, and Ö.L. Gülder, *The flame preheating effect on numerical modelling of soot formation in a two-dimensional laminar ethylene–air diffusion flame*, Combust. Theor. Model. 6 (2002), pp. 173–187.

[18] M. Fairweather, W.P. Jones, and R.P. Lindstedt, *Predictions of radiative transfer from a turbulent reacting jet in a cross-wind*, Combust. Flame 89 (1992), pp. 45–63.

[19] K.M. Leung, R.P. Lindstedt, and W.P. Jones, *A simplified reaction mechanism for soot formation in nonpremixed flames*, Combust. Flame 87 (1991), pp. 289–305.

[20] B.G. Carlson and K.D. Lathrop, *Transport theory – The method of discrete ordinates*, in *Computing Methods in Reactor Physics*, H. Greenspan, C.N. Kelber, and D. Okrent, eds., Gordon and Breach, London, 1968, pp. 171–266.
[21] F. Liu, G.J. Smallwood, and Ö.L. Gülder, *Band lumping strategy for radiation heat transfer calculations using a narrowband model*, J. Thermophys. Heat Transfer 14 (2000), pp. 278–281.
[22] S.V. Patankar, *Numerical Heat Transfer and Fluid Flow*, Taylor & Francis, London, 1980.
[23] Z. Liu, C. Liao, C. Liu, and S. McCormick, *Multigrid method for multi-step finite rate combustion*, AIAA paper 95-0205 (1995).
[24] Q. Zhang, H. Guo, F. Liu, G.J. Smallwood, and M.J. Thomson, *Implementation of an advanced fixed sectional aerosol dynamics model with soot aggregate formation in a laminar methane/air coflow diffusion flame*, Combust. Theor. Model. 12 (2008), pp. 621–641.
[25] M.S. Day and J.B. Bell, *Numerical simulation of laminar reacting flows with complex chemistry*, Combust. Theor. Model. 4 (2000), pp. 535–556.
[26] R.B. Pember, L.H. Howell, J.B. Bell, P. Colella, W.Y. Crutchfield, W.A. Fiveland, and J.P. Jessee, *An adaptive projection method for unsteady, low-Mach number combustion*, Combust. Sci. Tech. 140 (1998), pp. 123–168.
[27] J.B. Bell, A.J. Aspden, M.S. Day, and M.J. Lijewski, *Numerical simulation of low Mach number reacting flows*, J. Phys: Conf. Ser. 78 (2007) doi: 10.1088/1742-6596/78/1/012004.
[28] S.A. Northrup and C.P.T. Groth, *Solution of laminar diffusion flames using a parallel adaptive mesh refinement algorithm*, 43rd AIAA Aerospace Sciences Meeting and Exhibit, Reno, Nevada, AIAA paper 2005-0547, 10–13 January, 2005.
[29] S.A. Northrup and C.P.T. Groth, *Solution of laminar combusting flows using a parallel implicit adaptive mesh refinement algorithm*, in *Proceedings of the Fourth International Conference on Computational Fluid Dynamics, ICCFD4*, Ghent, Belgium, 10–14 July, 2006, pp. 341–346.
[30] K.K. Kuo, *Principles of Combustion*, 2nd edn, John Wiley, New Jersey, 2005.
[31] J.O. Hirschfelder, C.F. Curtiss, and R.B. Byrd, *Molecular Theory of Gases and Liquids*, John Wiley, New York, 1969.
[32] I.M. Kennedy, W. Kollmann, and J.Y. Chen, *A model for the soot formation in a laminar diffusion flame*, Combust. Flame 81 (1990), pp. 73–85.
[33] A. Gomez and D.E. Rosner, *Thermophoretic effects on particles in counterflow laminar diffusion flames*, Combust. Sci. Tech. 89 (1993), pp. 335–362.
[34] J. Nagle and R.F. Strickland-Constable, *Oxidation of carbon between 1000–2000°C*, in *Proceedings of the Fifth Conference on Carbon*, Pergamon Press, London, 1962, pp. 154–164.
[35] J.B. Moss, C.D. Stewart, and K.J. Young, *Modeling soot formation and burnout in a high temperature laminar diffusion flame burning under oxygen-enriched conditions*, Combust. Flame 101 (1995), pp. 491–500.
[36] D. Bradley, G. Dixon-Lewis, S.E. Habik, and E.M.J. Mushi, *The oxidation of graphite powder in flame reaction zones*, Proc. Combust. Inst. 20 (1984), pp. 931–940.
[37] O.A. Ezekoye and Z. Zhang, *Soot oxidation and agglomeration modeling in a microgravity diffusion flame*, Combust. Flame 110 (1997), pp. 127–139.
[38] R. Viskanta and M.P. Mengüç, *Radiation heat transfer in combustion systems*, Prog. Energy Combust. Sci. 13 (1987), pp. 97–160.
[39] A.A. Lacis and V. Oinas, *A description of the correlated k distribution method for modeling nongray gaseous absorption, thermal emission, and multiple scattering in vertically inhomogeneous atmospheres*, J. Geophys. Res. 96 (1991), pp. 9027–9063.
[40] C.P. Thurgood, A. Pollard, and H.A. Becker, *TN quadrature set for the discrete ordinates method*, J. Heat Transfer 117 (1995), pp. 1068–1070.
[41] S. Jendoubi, H.S. Lee, and T.K. Kim, *Discrete ordinates solutions for radiatively participating media in a cylindrical enclosure*, J. Thermophys. Heat Transfer 7 (1993), pp. 213–219.
[42] A. Soufiani and J. Taine, *High temperature gas radiative property parameters of statistical narrow-band model for H_2O, CO_2 and CO, and correlated-K model for H_2O and CO_2*, Int. J. Heat Mass Transfer 40 (1997), pp. 987–991.
[43] F. Liu, G.J. Smallwood, and Ö.L. Gülder, *Application of the statistical narrow-band correlated-k method to non-grey gas radiation in CO_2-H_2O mixtures: Approximate treatments of overlapping bands*, J. Quant. Spectrosc. Radiat. Transfer 68 (2001), pp. 401–417.

[44] V. Goutière, A. Charette, and L. Kiss, *Comparative performance of nongray gas modeling techniques*, Numer. Heat Transfer, Part B 41 (2002), pp. 361–381.
[45] M.F. Modest, *Radiative Heat Transfer*, 2nd edn, Academic Press, New York, 2003.
[46] S.A. Northrup and C.P.T. Groth, *Parallel implicit adaptive mesh refinement algorithm for solution of laminar combusting flows*, in *Proceedings of the 14th Annual Conference of the CFD Society of Canada*, Kingston, Ontario, Canada, paper 1106, 16–18 July 2006, pp. 221–228.
[47] X. Gao and C.P.T. Groth, *Parallel adaptive mesh refinement scheme for turbulent non-premixed combusting flow prediction*, 44th AIAA Aerospace Sciences Meeting and Exhibit, Reno, Nevada, Vol. 23, AIAA paper 2006-1448, 9–12 January 2006, pp. 17450–17463.
[48] S. Venkateswaran and C.L. Merkle, *Analysis of preconditioning methods for the Euler and Navier–Stokes equations*, Von Karman Institute Lecture Series, 1999.
[49] J.M. Weiss and W.A. Smith, *Preconditioning applied to variable and constant density flows*, AIAA J. 33 (1995), pp. 2050–2057.
[50] J.M. Weiss, J.P. Maruszewski, and W.A. Smith, *Implicit solution of preconditioned Navier–Stokes equations using algebraic multigrid*, AIAA J. 37 (1999), pp. 29–36.
[51] Y.-H. Choi and C.L. Merkle, *The application of preconditioning in viscous flows*, J. Comput. Phys. 105 (1993), pp. 207–223.
[52] S.K. Godunov, *Fintite-difference method for numerical computations of discontinuous solutions of the equations of fluid dynamics*, Mat. Sb. 47 (1959), pp. 271–306.
[53] P.L. Roe, *Approximate Riemann solvers, parameter vectors, and difference schemes*, J. Comput. Phys. 43 (1981), pp. 357–372.
[54] P.L. Roe and J. Pike, *Efficient construction and utilisation of approximate Riemann solutions*, in *Computing Methods in Applied Science and Engineering*, Vol. VI, R. Glowinski and J.L. Lions, eds., North-Holland, Amsterdam, 1984, pp. 499–518.
[55] A. Harten, *High resolution schemes for hyperbolic conservation laws*, J. Comput. Phys. 49 (1983), pp. 357–393.
[56] J.S. Shuen, *Inviscid flux-splitting algorithms for real gases with non-equilibrium chemistry*, J. Comput. Phys. 90 (1990), pp. 371–395.
[57] R. Walters, P. Cinnella, D. Slack, and D. Halt, *Characteristic-based algorithms for flows in thermochemical nonequilibrium*, AIAA J. 30 (1992), pp. 1304–1313.
[58] B. Engquist and S. Osher, *One-sided difference approximations for nonlinear conservation laws*, Math. Comp. 36 (1981), pp. 321–352.
[59] B. van Leer, *Towards the ultimate conservative difference scheme. V. A second-order sequel to Godunov's method*, J. Comput. Phys. 32 (1979), pp. 101–136.
[60] V. Venkatakrishnan, *Convergence to steady state solutions of the Euler equations on unstructured grids with limiters*, J. Comput. Phys. 118 (1995), pp. 120–130.
[61] T.J. Barth and D.C. Jespersen, *The design and application of upwind schemes on unstructured meshes*, AIAA Paper 89-0366, 1989.
[62] W.J. Coirier, *An adaptively-refined, Cartesian, cell-based scheme for the Euler and Navier–Stokes equations*, PhD thesis, University of Michigan, 1994.
[63] W.J. Coirier and K.G. Powell, *Solution-adaptive Cartesian cell approach for viscous and inviscid flows*, AIAA J. 34 (1996), pp. 938–945.
[64] D.W. Zingg and M. Yarrow, *A method of smooth bivariate interpolation for data given on a generalized curvilinear grid*, SIAM J. Sci. Stat. Comput. 13 (1992), pp. 687–693.
[65] C.P.T. Groth and S.A. Northrup, *Parallel implicit adaptive mesh refinement scheme for body-fitted multi-block mesh*, 17th AIAA Computational Fluid Dynamics Conference, Toronto, Ontario, Canada, AIAA paper 2005-5333, 6–9 June 2005.
[66] Y. Saad and M.H. Schultz, *GMRES: A generalized minimal residual algorithm for solving nonsymmetric linear systems*, SIAM J. Sci. Stat. Comput. 7 (1986), pp. 856–869.
[67] Y. Saad, *Krylov subspace methods on supercomputers*, SIAM J. Sci. Stat. Comput. 10 (1989), pp. 1200–1232.
[68] P.N. Brown and Y. Saad, *Hybrid Krylov methods for nonlinear systems of equations*, SIAM J. Sci. Stat. Comput. 11 (1990), pp. 450–481.
[69] Y. Saad, *Iterative Methods for Sparse Linear Systems*, PWS Publishing Company, Boston, 1996.
[70] D.A. Knoll and D.E. Keyes, *Jacobian-free Newton–Krylov methods: A survey of approaches and applications*, J. Comput. Phys. 193 (2004), pp. 357–397.

[71] R.S. Dembo, S.C. Eisenstat, and T. Steihaug, *Inexact Newton methods*, SIAM J. Numer. Anal. 19 (1982), pp. 400–408.
[72] W.A. Mulder and B. van Leer, *Experiments with implicit upwind methods for the Euler equations*, J. Comput. Phys. 59 (1985), pp. 232–246.
[73] J.S. Sachdev, C.P.T. Groth, and J.J. Gottlieb, *A parallel solution-adaptive scheme for multi-phase core flows in solid propellant rocket motors*, Int. J. Comput. Fluid Dyn. 19 (2005), pp. 159–177.
[74] J.S. Sachdev and C.P.T. Groth, *A mesh adjustment scheme for embedded boundaries*, Commun. Comput. Phys. 2 (2007), pp. 1095–1124.
[75] X. Gao and C.P.T. Groth, *Parallel adaptive mesh refinement scheme for three-dimensional turbulent non-premixed combustion*, 46th AIAA Aerospace Sciences Meeting and Exhibit, Reno, Nevada, AIAA paper 2008-1017, 7–10 January, 2008.
[76] M.J. Berger, *Adaptive mesh refinement for hyperbolic partial differential equations*, J. Comput. Phys. 53 (1984), pp. 484–512.
[77] M.J. Berger and P. Colella, *Local adaptive mesh refinement for shock hydrodynamics*, J. Comput. Phys. 82 (1989), pp. 67–84.
[78] M.J. Berger and J.S. Saltzman, *AMR on the CM-2*, Appl. Numer. Math. 14 (1994), pp. 239–253.
[79] M.J. Aftomis, M.J. Berger and J.E. Melton, *Robust and efficient Cartesian mesh generation for component-base geometry*, AIAA J. 36 (1998), pp. 952–960.
[80] J.J. Quirk, *An adaptive grid algorithm for computational shock hydrodynamics*, PhD thesis, Cranfield Institute of Technology, 1991.
[81] D. de Zeeuw and K.G. Powell, *An adaptively refined Cartesian mesh solver for the Euler equations*, J. Comput. Phys. 104 (1993), pp. 56–68.
[82] J.J. Quirk and U.R. Hanebutte, *A parallel adaptive mesh refinement algorithm*, ICASE Report 93-63, 1993.
[83] W. Gropp, E. Lusk, and A. Skjellum, *Using MPI*, MIT Press, Cambridge, MA, 1999.
[84] J. Gonçalves and P.J. Coelho, *Parallelization of the discrete ordinates method*, Numer. Heat Transfer, Part B 32 (1997), pp. 151–173.
[85] L.H. Howell, *A parallel AMR implementation of the discrete ordinates method for radiation transport*, in *Adaptive Mesh Refinement – Theory and Applications*, Lecture Notes in Computational Science and Engineering, Vol. 41, T. Plewa, T. Linde, and V.G. Weirs, eds., Springer, Berlin, 2005, pp. 255–270.
[86] M.R.J. Charest, C.P.T. Groth, and Ö.L. Gülder, *Solution of the equation of radiative transfer using a Newton–Krylov approach and adaptive mesh refinement*, Submitted to the Journal of Computational Physics, 2010.
[87] E. Turkel, R. Radespiel, and N. Kroll, *Assessment of preconditioning methods for multidimensional aerodynamics*, Comput. Fluids 26 (1997), pp. 613–634.
[88] D.G. Goodwin, *An open-source, extensible software suite for CVD process simulation*, Chemical Vapor Deposition XVI and EUROCVD 14, 2003, pp. 155–162.
[89] F. Liu, H. Guo, and G.J. Smallwood, *Effects of radiation model on the modeling of a laminar coflow methane/air diffusion flame*, Combust. Flame 138 (2004), pp. 136–154.
[90] G.P. Smith, D.M. Golden, M. Frenklach, N.W. Moriarty, B. Eiteneer, M. Goldenberg, C.T. Bowman, R.K. Hanson, S. Song, W.C. Gardiner, Jr., V.V. Lissianski, and Z. Qin, *GRI-Mech 3.0*, 2002. http://www.me.berkeley.edu/gri_mech/.
[91] D.R. Snelling, K.A. Thomson, G.J. Smallwood, and Ö.L. Gülder, *Two-dimensional imaging of soot volume fraction in laminar diffusion flames*, Appl. Opt. 38 (1999), pp. 2478–2485.
[92] C.K. Law, *Comprehensive description of chemistry in combustion modeling*, Combust. Sci. Tech. 177 (2005), pp. 845–870.
[93] Z. Qin, V.V. Lissianski, H. Yang, W.C. Gardiner, S.G. Davis, and H. Wang, *Combustion chemistry of propane: A case study of detailed reaction mechanism optimization*, Proc. Combust. Inst. 28 (2000), pp. 1663–1669.
[94] R. Bustinza, G.N. Gatica, and B. Cockburn, *An a posteriori error estimate for the local discontinuous Galerkin method applied to linear and nonlinear diffusion problems*, J. Sci. Comput. 22–23 (2005), pp. 147–185.
[95] M. Nemec, M.J. Aftosmis, and M. Wintzer, *Adjoint-based adaptive mesh refinement for complex geometries*, AIAA Paper 2008-0725, 2008.
[96] F.N. Egolfopoulos and P.E. Dimotakis, *A comparative numerical study of premixed and non-premixed ethylene flames*, Combust. Sci. Tech. 162 (2001), pp. 19–35.

[97] A. Kazakov and M. Frenklach, *Reduced reaction sets based on GRI-Mech 1.2*, 1994. http://www.me.berkeley.edu/drm/.

[98] J. Appel, H. Bockhorn, and M. Frenklach, *Kinetic modeling of soot formation with detailed chemistry and physics: Laminar premixed flames of C_2 hydrocarbons*, Combust. Flame 121 (2000), pp. 122–136.

[99] G. Amdahl, *Validity of the single processor approach to achieving large-scale computing capabilities*, AFIPS '67 (Spring): Proceedings of the Spring Joint Computer Conference, April 18–20, 1967, pp. 483–485.